9594–9609 *Nucleic Acids Research, 2023, Vol. 51, No. 18* *Published online 13 September 2023*
https://doi.org/10.1093/nar/gkad756

CRISPR screens in sister chromatid cohesion defective cells reveal PAXIP1-PAGR1 as regulator of chromatin association of cohesin

Janne J.M. van Schie[1,2,†], Klaas de Lint[1,2,†], Thom M. Molenaar[1,2], Macarena Moronta Gines[3], Jesper A. Balk[1,2], Martin A. Rooimans[1,2], Khashayar Roohollahi[1,2], Govind M. Pai[1,2], Lauri Borghuis[1,2], Anisha R. Ramadhin[1,2], Francesco Corazza[3], Josephine C. Dorsman[1,2], Kerstin S. Wendt[3], Rob M.F. Wolthuis[1,2] and Job de Lange[1,2,*]

[1]Amsterdam UMC location Vrije Universiteit Amsterdam, Department of Human Genetics, Section Oncogenetics, Amsterdam, The Netherlands, [2]Cancer Center Amsterdam, Cancer Biology and Immunology, Amsterdam, The Netherlands and [3]Erasmus Medical Centre, Department of Cell Biology, Rotterdam, The Netherlands

Received January 19, 2023; Revised August 22, 2023; Editorial Decision August 24, 2023; Accepted September 05, 2023

ABSTRACT

The cohesin complex regulates higher order chromosome architecture through maintaining sister chromatid cohesion and folding chromatin by DNA loop extrusion. Impaired cohesin function underlies a heterogeneous group of genetic syndromes and is associated with cancer. Here, we mapped the genetic dependencies of human cell lines defective of cohesion regulators DDX11 and ESCO2. The obtained synthetic lethality networks are strongly enriched for genes involved in DNA replication and mitosis and support the existence of parallel sister chromatid cohesion establishment pathways. Among the hits, we identify the chromatin binding, BRCT-domain containing protein PAXIP1 as a novel cohesin regulator. Depletion of PAXIP1 severely aggravates cohesion defects in ESCO2 mutant cells, leading to mitotic cell death. PAXIP1 promotes global chromatin association of cohesin, independent of DNA replication, a function that cannot be explained by indirect effects of PAXIP1 on transcription or DNA repair. Cohesin regulation by PAXIP1 requires its binding partner PAGR1 and a conserved FDF motif in PAGR1. PAXIP1 co-localizes with cohesin on multiple genomic loci, including active gene promoters and enhancers. Possibly, this newly identified role of PAXIP1-PAGR1 in regulating cohesin occupancy on chromatin is also relevant for previously described functions of PAXIP1 in transcription, immune cell maturation and DNA repair.

GRAPHICAL ABSTRACT

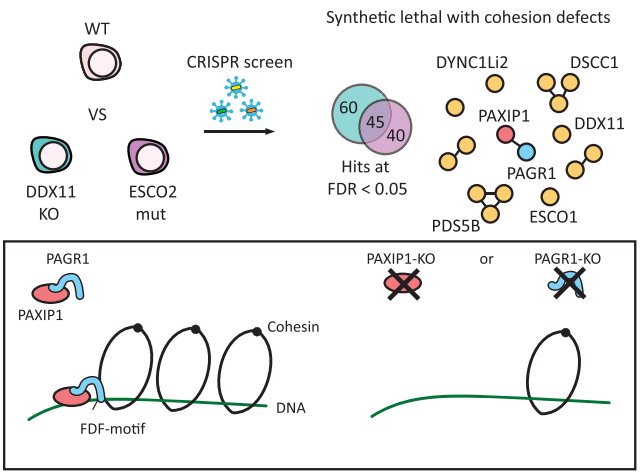

INTRODUCTION

The cohesin complex regulates structural genome organization, thereby contributing to critical cellular processes including transcription, DNA repair and chromosome segregation. The SMC1/SMC3 heterodimer, the kleisin subunit RAD21 and one SA subunit (SA1 or SA2) together form a circular structure that can physically tether DNA molecules (1). This occurs *in trans*, to facilitate chromosome

*To whom correspondence should be addressed. Tel: +31 204448283; Email: j.delange1@amsterdamumc.nl
†The authors wish it to be known that, in their opinion, the first two authors should be regarded as Joint First Authors.

segregation and homology directed DNA repair, and *in cis*, to create chromatin loops that can form topologically associating domains (TADs) and play roles in transcriptional regulation (2). While required for sister chromatid cohesion, topological DNA entry into the ring may not be needed for cohesin's role in loop extrusion (3). Defective cohesin function and mutations in cohesin genes and regulators are associated with cancer (4) and underlie a group of rare developmental disorders, termed cohesinopathies (5).

The establishment of sister chromatid cohesion is tightly coupled to DNA replication (6). Cohesion establishment depends on the acetylation of SMC3 by ESCO2 during DNA replication to promote the association of Sororin, which counteracts cohesin dissociation by the cohesin release factor WAPL (7–10). In addition, several other replisome associated proteins are involved. Based on epistasis studies in yeast, these are suggested to function in two parallel pathways (11,12). One pathway requires Chl1, Csm3-Tof1 and Ctf4 (DDX11, TIMELESS-TIPIN and AND-1 in human) and is believed to depend on cohesin complexes that were pre-loaded onto chromatin in G1 (13). The second pathway involves the alternative PCNA loader subunits Ctf18-Ctf8-Dcc1 (CHTF18-CHTF8-DSCC1 in human) and depends on *de novo* loading of cohesin during DNA replication by Scc2 (NIPBL in human) (13). To what extent these findings in yeast also apply to human cells, and which additional factors contribute to cohesion establishment, remains to be determined.

Although sister chromatid cohesion is essential for cellular proliferation, partial loss of cohesion can be tolerated to different degrees. Cell lines derived from patients with the cohesinopathies Warsaw Breakage Syndrome and Roberts Syndrome, caused by mutations in the DNA helicase DDX11 and the acetyltransferase ESCO2, respectively, are both characterized by premature loss of cohesion in metaphase. While these cells are viable, this phenotype creates specific vulnerabilities. Combined impairment of redundant cohesion establishment pathways is synthetically lethal due to enhanced cohesion defects beyond tolerable levels (11,12,14–16). Moreover, cohesion defects and inactivating mutations in cohesion related genes can sensitize cells to prolonged metaphase duration and drugs that induce DNA damage (17–24). Identification of the factors that determine cohesion proficiency may be clinically relevant, as they point at potential vulnerabilities of cohesion defective cancer cells (23).

Only a fraction of chromatin-bound cohesin maintains sister chromatid cohesion (25,26), while cohesin also contributes to intra-chromosomal DNA-DNA contacts. Cohesin occupancy on chromatin is regulated by the dynamic loading, translocation and unloading of cohesin. The NIPBL-MAU2 heterodimer loads cohesin onto DNA, while WAPL promotes release of cohesin from chromatin. NIPBL-bound cohesin mediates active DNA loop extrusion to fold DNA fibers (27,28), thereby contributing to 3D chromosome organization and *in cis* DNA–DNA contacts including enhancer-promotor loops involved in transcriptional regulation (2). CCCTC-binding factor (CTCF) can anchor cohesin translocation by interacting with cohesin via a conserved F/YxF motif, thereby enriching cohesin occupancy at CTCF sites and stabilizing cohesin onto chromatin by restricting WAPL binding (29). In addition, various other chromatin-binding proteins, including chromatin remodelers, are reported to interact with and enrich cohesin and/or its loader at specific chromatin sites (30–37). Thereby, spatiotemporal cohesin occupancy on chromatin is tightly coordinated with and influenced by chromatin dynamics.

In this study, we aimed to map the human genes involved in modulating sister chromatid cohesion and to find mechanisms of tolerance against partial sister chromatid cohesion loss. By using genome-wide CRISPR screens in DDX11 and ESCO2 defective human cell lines, we generated a network of synthetic lethal interactors of cohesion loss. Among our hits we identified the chromatin associated PAXIP1-PAGR1 complex as a novel regulator of cohesin association with chromatin.

MATERIALS AND METHODS

Cell culture

All cell lines were maintained in Dulbecco's modified Eagle's medium (DMEM, Gibco) with 9% FCS, 1 mM sodium pyruvate (Gibco) and penicillin–streptomycin (Gibco). RPE1-hTert-TetonCas9-PuroKO-TP53KO cells, referred to as RPE1-WT throughout this manuscript, were described previously (38). HCT116-KMT2D-KO cells were a kind gift from Yiping He (39).

CRISPR-Cas9 gene editing

For CRISPR-Cas9 based gene editing approaches, we used an inducible Tet-On Cas9 expression system in combination with transfection of synthetic crRNA (IDT). In short, Cas9 expression was induced by 200 ng/ml doxycycline followed by transfection with 20 nM equimolar crRNA:tracrRNA duplexes with 1:1000 RNAiMax (Life Technologies). Genomic DNA was isolated with direct PCR lysis reagent (Viagen Biotech) with Proteinase K (O/N 55°C). Proteinase K was inactivated (20 min 82°C) and the crRNA target site was amplified with One Taq Hot Start DNA polymerase kit (NEB), followed by Sanger sequencing (primers in Supplementary Table S3). Gene editing efficiencies were assessed using the Synthego ICE analysis tool (40).

Genome-wide CRISPR-Cas9 screens

Genome-wide CRISPR-Cas9 screens were performed with the TKOv3 library (41) in triplicate at 400-fold library representation as previously described (38). In short, cells were transduced at MOI 0.2 with lentiviral pLCKO-TKOv3 and 8 μg/ml polybrene, and selected for viral integration with 5 μg/ml puromycin for three days. Cells were then harvested to take a t = 0 sample and reseeded with 200 ng/ml doxycycline to induce Cas9 expression. After every 3 population doublings, cells were passaged for a total of 12 population doublings with doxycycline. Genomic DNA was isolated using the Blood and Cell Culture DNA Maxi Kit (Qiagen) and integrated gRNA sequences were amplified by PCR using HiFi HotStart ReadyMix (KAPA). Resulting PCR products were used as a template in a second PCR reaction in which Illumina adapters and barcodes were added.

Samples were pooled and sequenced on an Illumina NovaSeq6000. Data was analyzed as described before (42) and as described in Supplementary Table S1. Briefly, sequencing reads were mapped to the TKOv3 library sequences with no mismatch tolerance. End-point reads were normalized to $t = 0$ values by multiplying the average $t = 0$ count per guide by the $t = 12/t = 0$ fold-change (pseudocount + 1), and the normalized counts were used as input for DrugZ analysis.

Flow cytometry based cell cycle assay

Cells were incubated for 10 min with 10 μM 5′-ethynyl-2′-deoxyuridine (EdU), harvested, fixed in 4% paraformaldehyde for 15 min and subsequently overnight in 70% EtOH at −20°C. Cells were then permeabilized in 0.5% Triton X-100, blocked with 5% FCS and incubated with histone H3 pS10 Alexa Fluor 647 in 1% BSA, followed by incubation for 30 min with Click-it reaction mixture (50 mM Tris–HCl pH 7.6, 150 mM NaCl, 4 mM $CuSO_4$, 1 μM picolyl azide 5/6-FAM, 2 mg/ml sodium-L-ascorbate) for EdU detection. Cells were washed and resuspended in 1% BSA with DAPI and detected by flow cytometry on a BD LSRFORTESSA X-20 (BD Biosciences). Data analysis was done using FlowJo V10.

Clonogenic and viability assays

Two days after transfection of crRNA:tracrRNA duplexes, 1000 cells/well were seeded in 6-wells plates for clonogenic assays and 500 cells/well in 96-well plates for CellTiter-Blue assays. For clonogenic assays, cells were fixed in 100% ice-cold MeOH 10 days after crRNA transfection, followed by staining in 0.5% crystal violet with 20% MeOH. CellTiter-Blue assays were performed 7 days after transfection. After incubation with CellTiter-Blue reagent (Promega) for 4 h at 37°C, fluorescence was measured at $560_{Ex}/590_{Em}$ with an Infinite F200 microplate reader (Tecan). For Incucyte experiments, cell growth was monitored at a 4 h interval by an Incucyte Zoom instrument (Essen Bioscience) with a 10× objective.

Two-color competitive growth assay

Cells were transduced with either NLS-mCherry-sgLacZ or NLS-GFP GOI-sgRNA and selected with 5 μg/ml puromycin. GFP and mCherry expressing cells were mixed in a 1:1 ratio and plated with 100 ng/ml doxycycline. Every 3–4 days, cells were passaged and GFP/mCherry proportions were determined by flow cytometry on a BD LSRFORTESSA X-20 (BD Biosciences).

Protein extraction and co-immunoprecipitation

RPE1 cells were lysed in buffer containing 50 mM Tris–HCl pH 7.4, 150 mM NaCl, 1% Triton X-100 and protease inhibitors (1 h on ice). Alternatively, where indicated, separate chromatin-bound and soluble protein fractions were prepared. First, cells were lysed in lysis buffer 1 (50 mM Tris–HCl pH 7,5; 150 mM NaCl; 10% glycerol; 0,2% NP-40) for 10 min on ice and centrifuged at 1300g for 10 min. Supernatant was used as soluble fraction. The pellet was then washed three times, followed by incubation in lysis buffer 2 (50 mM Tris–HCl pH 7,5; 150 mM NaCl; 10% glycerol; 1,0% NP-40 + 5 mM $MgCl_2$ + 5 units/μl Benzonase) for 2 h on ice, centrifuged at max speed for 5 min and the supernatant was used as chromatin-bound fraction. For co-immunoprecipitation, 3.5 million cells were seeded in two 15 cm dishes 48 h prior to harvest. Venus-tagged PAXIP1 was precipitated from chromatin-bound protein fractions using GFP-trap beads (Chromotek; gta-20) following the manufacturer's protocol. Beads were washed 7× and protein was eluted in sample buffer.

For western blots, proteins were separated using 4–15% Mini-PROTEAN Precast Protein gels (BioRad) and transferred to Immobilon-P PVDF membrane (Millipore). After blocking in 5% dry milk in TBST-T, membranes were incubated in primary and subsequently secondary peroxidase conjugated antibodies (antibodies used are listed in Supplementary Table S3). Protein bands were visualized by incubation with ECL prime (Amersham).

ChIP-qPCR

Chromatin immunoprecipitation was performed as described (43). In brief, cells were crosslinked with formaldehyde, lysed and sonicated (Diagenode Bioruptor, Seraing, Belgium). The pull-down was performed with anti-RAD21 (Abcam ab154769) and rabbit control IgG (Diagenode C15410206) using Protein G dynabeads (Thermo Scientific 10004D). The qPCR was performed using the Applied Biosystems SYBR Select Master Mix for CFX (Thermo Scientific 4472942) and the CFX96 C1000 Thermal cycler (Bio-Rad) using the qPCR primers listed in Supplementary Table S3.

Immunofluorescence

Cells were grown on coverslips, pre-extracted with 0.5% Triton X-100 (2 min RT) where indicated and fixed in 4% paraformaldehyde. After permeabilization in 0.3% Triton X-100, cells were blocked in blocking buffer (3% BSA, 0.3% Triton X-100 in PBS), incubated with the indicated antibodies diluted 1:500 in blocking buffer, washed three times with PBS and incubated with appropriate anti-mouse/rabbit Cy3 conjugated antibody. After washing with PBS 3 times, coverslips were mounted with DAPI gold antifade (Invitrogen). Images were acquired using fluorescence microscopy (Leica). Analysis was performed using ImageJ. Background was subtracted using rolling ball background subtraction before quantification of nuclear intensity.

Cohesion defect analysis

Cells were treated with 200 ng/ml democolcin for 20 min, harvested and resuspended in 0.075 mM KCl for 20 min. Next, cells were fixed in 3:1 methanol:acetic acid, dropped onto glass slides and stained in 5% Giemsa solution. For each condition 50 metaphases from coded slides were assessed for railroad chromosomes and premature chromatid separation. Metaphases were scored as normal with 0–4 railroad chromosomes, as partially separated with 5–10 railroad chromosomes and as single chromatids with at least two chromosomes completely separated.

Time-lapse microscopy

Cells were seeded in a 96-wells plate with 1 μM SiR-DNA and 10 μM verapamil (Spirochrome) and imaged every three minutes with a microscope (ImageXpress Pico) in a heated culture chamber (5% CO_2 at 37 °C).

siRNA experiments

For siRNA experiments, cells were transfected with 20 nM siRNA using 1:1000 RNAiMAX and analyzed after 48 h, unless otherwise stated.

Lentiviral constructs and transduction

DDX11 and empty vector expression constructs were previously described (20). To generate PAXIP1 and ESCO2 expression constructs, cDNA from RPE1 cells was cloned into pLenti CMVie-IRES-BlastR (Addgene plasmid #119863). PAXIP1 W75R, W175R and W676A mutants were constructed using overlap extension PCR. PAGR1 cDNA from HEK293T cells was N-terminally tagged with FLAG and cloned into pLenti CMVie-IRES-BlastR and in pLenti CMVie-IRES-PuroR. To reduce ectopic expression of PAGR1, the promoter region and 5′UTR of *PAGR1* (–324/+351 relative to NM_024516.4) and the promoter regions for *PGK1* (–421/+80 relative to NM_000291.4) and *UBC* (–334/+66 relative to NM_021009.7) were PCR amplified from RPE1 genomic DNA and cloned in front of FLAG-tagged PAGR1 cDNA (replacing the existing CMV promoter) in pLenti CMVie-IRES-PuroR. A minimal CMV promoter (GGTAGGCGTGTACGGTGGGAGGCCTATATAAGCAGAGCTCGTTTAGTGAACCGTCAGATCGCC) was also used for comparison. Lentiviral particles were produced in HEK293T cells and transduced into the indicated RPE1 cell lines, followed by selection with 10 μg/ml blasticidin or 5 μg/ml puromycin (Invitrogen).

RNA-seq

Total RNA was isolated using the RNeasy mini kit (Qiagen). Up to 5 × 10^6 cells per sample were lysed in RLT buffer. Samples were enriched for mRNA using the KAPA mRNA Hyperprep kit (Roche) and prepared for sequencing using the TruSeq RNA Library Prep Kit v2 (Illumina) according to the manufacturer's instructions, and sequenced on an Illumina HiSeq4000. The Fastq files were clipped and cleaned by fastp (44). The clipped Fastqs were mapped to the human reference genome (hg19) by HISAT2 alignment tool (45). SAM to BAM transformation as well as sorting and indexing were carried out by SAMtools (46). Subsequently, the gene-level raw reads were counted by Subread's featureCounts (47). Multi-mapping reads were also counted via assigning fractional counting to the genes. The raw count matrix was normalized and the differential expression analysis was performed by edgeR (48). The original library size was normalized to the effective library size by trimmed mean of M-value (TMM), followed by estimating dispersion by fitting the generalized linear model (GLM) with the design matrix. Subsequently, likelihood ratio test was performed to examine the differential expressions between WT and PAXIP1-KO samples. Differential expression with false discovery rate (FDR) < 0.05 was defined as significant.

ENCODE ChIP-seq data analysis

DeepTools (Version 3.5.1) (49) was used to generate heatmaps of publicly available ENCODE ChIP-seq data from HepG2 cells. Regions with peak summits (bed files) for RAD21 (ENCODE accession ENCFF052UCF), PAXIP1 (ENCFF825TUP), or POLR2A (ENCFF354VWZ) were sorted on signal (bigWig file) for RAD21 (ENCFF047SRI), PAXIP1 (ENCFF080TDD) or POLR2A (ENCFF425QWO), respectively, in a 2 kb window using computeMatrix (–referencePoint –referencePoint = center – beforeRegionStartLength = 1000 – beforeRegionStartLength = 1000 –sortRegions = descend). Similarly, to look at active enhancers versus promoters, regions with p300 (EP300) peaks (ENCFF827LSX) were sorted on H3K4me1 signal (ENCFF470RYT) in a 4kb window. Sorted bed files for RAD21, PAXIP1, POLR2A, or p300 were used to generate matrices with bigWig files from ChIP-seq signals for CTCF (ENCFF938HDS), p300 (ENCFF962CGI), H3K4me3 (ENCFF359LQU) and/or H3K4me1 (ENCFF470RYT) using computeMatrix (–sortRegions = keep). Heatmaps were generated using the plotHeatmap tool (–sortUsing = mean –sortRegions = keep).

RESULTS

Isogenic genome-wide CRISPR screens identify known and novel genetic interactors of DDX11 and ESCO2

To identify synthetic interactions in cells with impaired cohesion establishment, we used RPE1-hTert-TP53KO cells with inducible Cas9 (38) (hereafter referred to as RPE1-WT) to create isogenic cell lines with mutations in DDX11 and ESCO2. We generated a DDX11-KO cell line, but were unable to generate a viable ESCO2-KO cell line, similar as reported previously (50). Instead, we used a hypomorphic ESCO2 mutant with a mutation in the PDM-A domain (Supplementary Figure S1A). In line with previous studies (51,52), this resulted in reduced ESCO2 protein levels that only become detectable after inhibition of the proteasome (Supplementary Figure S1B). The resulting DDX11-KO and ESCO2-mut cell lines show no detectable DDX11 and strongly reduced ESCO2 levels, respectively (Figure 1A), and display pronounced cohesion defects (Figure 1B), confirming their functional impairment.

DDX11-KO, ESCO2-mut and WT cell lines were transduced with the genome-wide TKOv3 library (53) and cultured for 12 population doublings, followed by genomic DNA isolation and sequencing of sgRNA inserts (Figure 1C). The results of the WT screen were published previously (38). After normalization based on t = 0 counts, we computed WT versus DDX11-KO and WT versus ESCO2-mut gene-level depletion scores using DrugZ (54) (Supplementary Table S1). With an FDR < 0.05 we identified 105 and 85 synthetic lethal interactions, respectively, of which 45 overlapped between the two screens (Figure 1D). The hits are enriched in genes involved in sister chromatid cohesion,

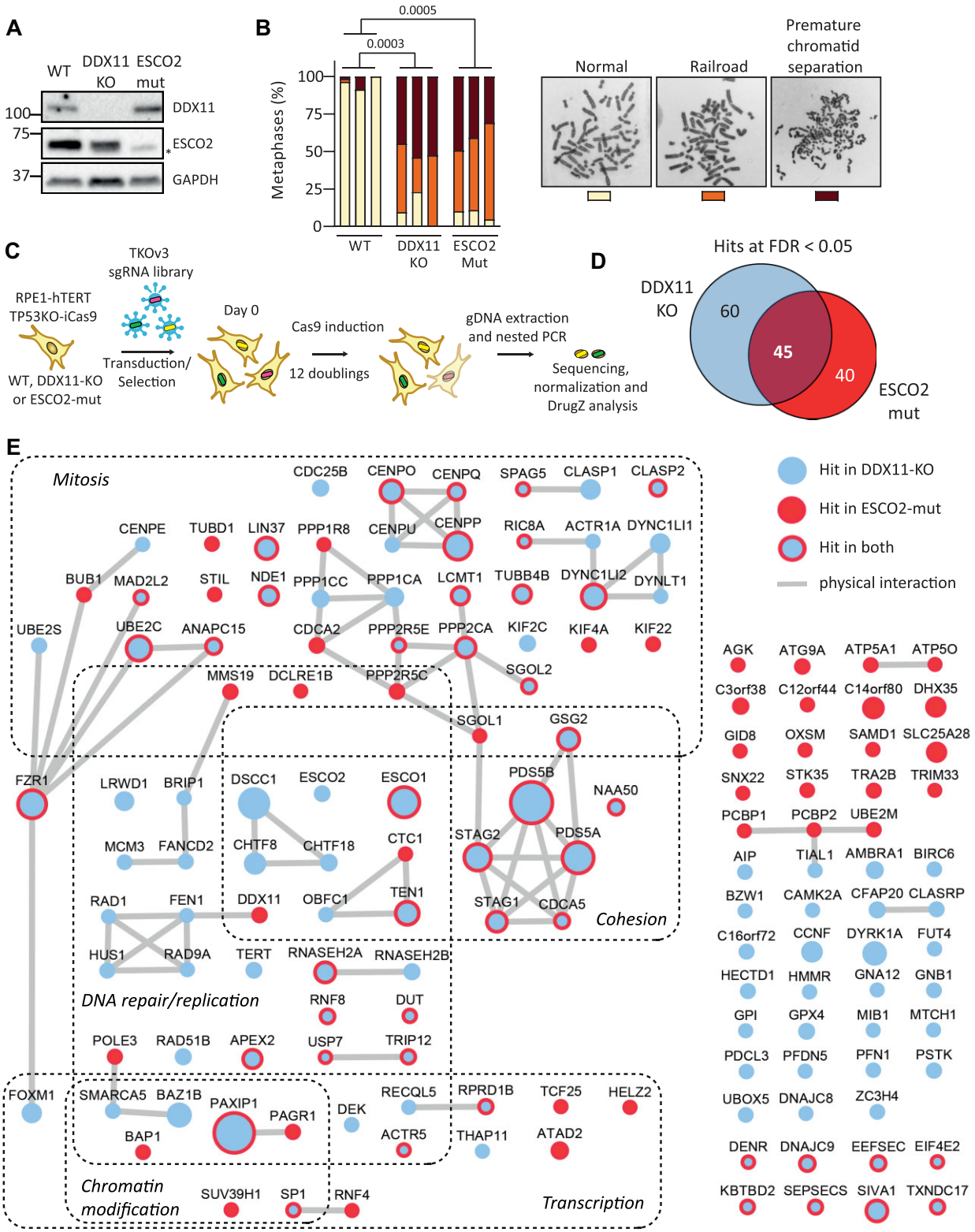

Figure 1. Genome-wide CRISPR screens identify genetic interactions with ESCO2 and DDX11. (**A**) Western blot of DDX11-KO and ESCO2-mutant cell lines. Asterisk indicates non-specific band. (**B**) Cohesion defect analysis of indicated cell lines. 50 metaphases were assessed for each sample, three independent experiments are shown as separate bars. *P*-values were calculated by a one-way ANOVA comparing the frequency of premature chromatid separation per condition. (**C**) Workflow of CRISPR screens, performed in triplicate. (**D**) Venn diagram of identified hits in both screens with FDR < 0.05 (DrugZ). (**E**) Network analysis of hits representing synthetically lethal genes with DDX11 (blue), ESCO2 (red) or both (blue-red). Edges indicate physical protein–protein interactions (String-db, evidence-based). Node size reflects significance, using the highest value from the two screens. Supplementary Table S1 contains the raw data.

mitosis and DNA replication and repair (Figure 1E and Supplementary Figure S1C). Both screens identified multiple previously described genetic dependencies, including synthetic lethality between DDX11 and ESCO2 (14,15) and the ESCO2 paralog ESCO1, which is particularly essential in ESCO2-mut cells (14,16,50). Similar as reported in budding yeast and vertebrate cell lines (11,24,42), DDX11-KO cells showed increased dependency on CHTF18, CHTF8 and DSCC1, the specific subunits of the alternative replication factor C clamp loader CHTF18-RFC. Moreover, in line with the role of DDX11 in mitigating DNA replication stress (18,20,55), DDX11-KO cells were particularly sensitive to depletion of multiple DNA replication and repair factors, such as BRIP1 (FANCJ), FANCD2, RAD51B and the RAD9A-HUS1-RAD1 (9–1–1) complex. Together, our screens yield high confidence networks of genetic dependencies of ESCO2 and DDX11, providing a rich resource of the human cohesin regulatory network.

To validate the identified synthetic lethal interactions, we reconstituted the knockout cell lines with ectopic DDX11 or ESCO2 (Supplementary Figure S2A-B). Subsequently, we depleted a selection of hits using Cas9 induction and either synthetic crRNA transfections (Figure 2) or viral sgRNA transductions (Supplementary Figure S2C, D) and assessed cell proliferation. This confirmed increased sensitivity to depletion of the cohesion factors ESCO1, ESCO2, DDX11, DSCC1, PDS5A and PDS5B. Remarkably, whereas ESCO2-mut cells are more sensitive to depletion of PDS5A than PDS5B, this is reversed in DDX11-KO cells, suggesting partially separate functions of the PDS5 homologs. In addition to known cohesion factors, the majority of other hits that we tested could also be validated, including PAXIP1, PAGR1, SIVA1, DYNC1Li2, BAZ1B, FZR1, RNF8, CENPP and CENPO, further confirming the high confidence of hits found in our screens.

As a representative mitosis-associated hit, we further analyzed the non-catalytic microtubule motor protein subunit DYNC1Li2. Knockdown of DDX11 and ESCO2 caused elevated mitotic fractions and cohesion loss in DYNC1Li2-KO cells compared to WT cells (Supplementary Figure S3). This suggests that while DYNC1Li2 does not seemingly play a pronounced role in cohesion in cells with intact sister chromatid cohesion, it becomes critical to mitigate further loss of cohesion in cohesion defective cells, possibly due to its role in metaphase duration, similar to what was previously shown for impaired APC/C function (23).

PAXIP1 promotes the chromatin association of cohesin

Among the top validated hits in the ESCO2 screen was PAXIP1, a chromatin binding protein with described functions in transcriptional regulation, the DNA damage response and immune cell maturation (56–58), but no described role in cohesin biology. In order to study PAXIP1 in more detail, we made clonal PAXIP1-KO RPE1 cells (Supplementary Figure S4A). Considering the role of PAXIP1 as a transcriptional regulator, we performed RNA sequencing (Supplementary Figure S4B-C and Table S2). While the expression of 664 genes was significantly changed in PAXIP1-KO cells (357 genes downregulated and 307 upregulated in PAXIP1-KO), no changes were observed in cohesin related genes or other hits from the CRISPR screen, suggesting that an altered transcriptional profile does not directly explain the observed synthetic lethality of PAXIP1 and ESCO2. An alternative explanation could lie in the role of PAXIP1 in the DNA damage response (59–61). However, we observed no increased γH2AX signaling in interphase (Supplementary Figure S4D). Of note, DNA damage could be observed upon PAXIP1 depletion in a fraction of ESCO2-mut cells with disrupted nuclear integrity (Supplementary Figure S4D), which is likely a secondary effect linked to mitotic catastrophe (62).

Interrogation of the DepMap database (https://depmap.org) revealed a remarkable correlation of essentiality of PAXIP1 with the cohesin subunits SMC3 and STAG2 and the loaders NIPBL and MAU2 (Supplementary Figure S4E). Since co-essentiality implies shared biological function (63), this led us to hypothesize that PAXIP1 may directly influence cohesin function. Although sister chromatid cohesion and cell cycle distribution were unaffected in PAXIP1-KO clones (Supplementary Figure S4F-G), we observed an aggravation of cohesion loss (Figure 3A) and accumulation of mitotic cells (Figure 3B) upon PAXIP1 depletion in ESCO2-mut cells, suggesting mitotic cell death resulting from detrimental cohesion defects. Strikingly, we detected reduced levels of chromatin-associated cohesin by RAD21 immunofluorescence in PAXIP1-KO cells (Figure 3C) and upon PAXIP1 knockdown (Supplementary Figure S4H). This was confirmed by ChIP-qPCR at several selected RAD21-binding sites (Supplementary Figure S5) and by immunoblotting RAD21, SMC3 and NIPBL in chromatin-bound protein fractions (Figure 3D and Supplementary Figure S4I). Chromatin-bound cohesin was reduced in both G1 and G2 synchronized cells (Figure 3D, Supplementary Figure S4J and Supplementary Figure S6), suggesting that this function of PAXIP1 is independent of DNA replication. Importantly, in line with the RNA-seq data, total levels of cohesin proteins were similar in WT and PAXIP1-KO cells (Figure 3D, Supplementary Figure S4I and Supplementary Figure S4K). Together, these results suggest that PAXIP1 directly influences the chromatin association of cohesin throughout the cell cycle.

PAXIP1 function in cohesin regulation depends on the interaction with PAGR1

PAXIP1 can physically associate with the histone methyltransferases KMT2C and KMT2D, the DNA damage response protein TP53BP1, and PAXIP1 associated glutamate-rich protein (PAGR1) (57,58,64–66). The ESCO2-mut CRISPR screen identified PAGR1, but not TP53BP1, KMT2C/D or any of the accessory subunits of the KMT2C/D methyltransferase complex (WDR5, RBBP5, ASH2L, DPY30, KDM6A) (Figure 1E and Supplementary Table S1). Co-depletion of KMT2C and KMT2D, which may in part be functionally redundant (67), also did not impair growth of ESCO2-mut cells (Supplementary Figure S7A-B), and chromatin-bound cohesin levels were not affected in KMT2C/D double KO (dKO) clones (Supplementary Figure S7C-F). Moreover, HCT116-KMT2D-KO cells (39), which already lack KMT2C (68), did not show a decrease in chromatin-bound

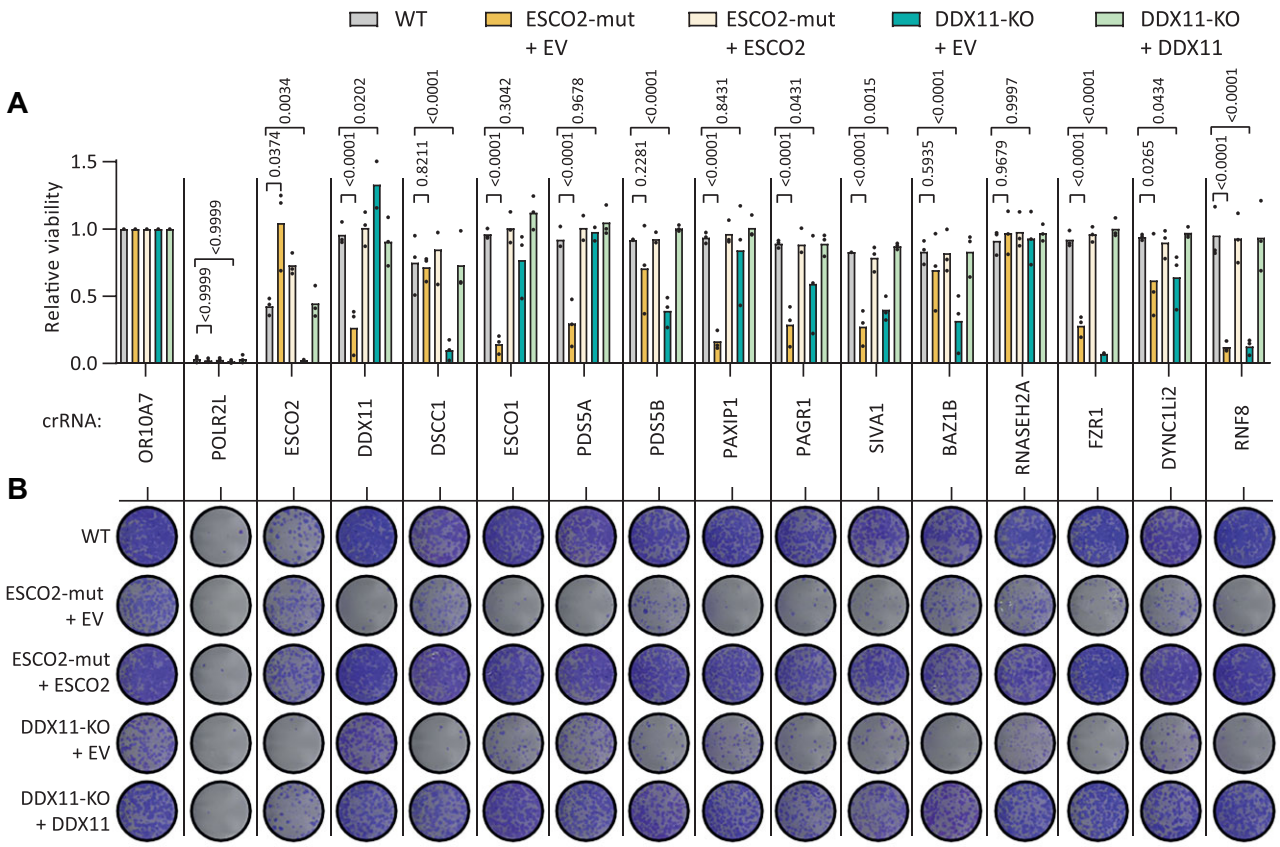

Figure 2. Hit validation in ESCO2-mut and DDX11-KO cells. (**A**) Viability of WT, ESCO2-mut and DDX11-KO cells assessed by a CellTiter-Blue assay, 7 days after crRNA:tracrRNA transfection and accompanying Cas9 induction. Viability is normalized to cells transfected with crOR10A7, a nonessential gene. POLR2L is used as a common essential control. Dots represent the mean of three technical replicates; bars indicate the mean of three independent experiments. P-values were calculated by a two-way ANOVA. (**B**) Clonogenic survival assay, 10 days after crRNA:tracrRNA transfection and Cas9 induction in indicated cells.

cohesin (Supplementary Figure S7G-H), further suggesting that KMT2C/D is not involved in regulating cohesin levels on chromatin.

Synthetic lethality of PAGR1 was validated by crRNA transfections, which resulted in increased lethality, cohesion defects and an elevated mitotic fraction in ESCO2-mut cells (Supplementary Figure S8A–C), similar as observed upon PAXIP1 depletion (Figure 3A, B). Next, we generated two PAGR1-KO clones using a crRNA targeting PAGR1 in its C terminal region (Supplementary Figure S8D). Although truncated protein products were still present (Figure 4A), PAGR1 protein was functionally impaired, illustrated by destabilized PAXIP1 protein levels as previously reported (57). Similar to PAXIP1-KO cells, PAGR1-KO cells showed decreased chromatin bound cohesin levels (Figure 4B, C) without causing cohesion defects in metaphase (Supplementary Figure S8E).

PAXIP1 has six BRCT (BRCA1 C-Terminus) domains that mediate the association with different interaction partners (57). To investigate which domains of PAXIP1 contribute to the chromatin association of cohesin, we reconstituted PAXIP1-KO cells with WT or mutant forms of PAXIP1 (Figure 4D). W75R is a BRCT1 mutant that does not abrogate PAGR1 binding but impairs the PAXIP1-PAGR1 sub-complex function, W165R perturbs the interaction with PAGR1, W676A with TP53BP1, and W929A and ΔBRCT5-6 were both reported to perturb the interaction of PAXIP1 with KMT2C/D (57,66). PAXIP1 mutants were expressed at levels similar to or higher than endogenous PAXIP1 (Figure 4E). This restored PAGR1 protein levels in PAXIP1-KO cells, except for the W165R mutant, in line with the reciprocal stabilization of PAXIP1 and PAGR1 following interaction (57). While PAXIP1-WT and W676A efficiently restored the level of chromatin-bound cohesin, no rescue was observed upon overexpression of W75R, W165R, W929A and ΔBRCT5-6 (Figure 4F). This suggests that (those residues within) BRCT1, BRCT2, BRCT5 and BRCT6, but not BRCT3, are required for the role of PAXIP1 in promoting chromatin association of cohesion. The fact that the W929A and ΔBRCT5-6 could not rescue the effects of PAXIP1-KO may suggest that BRCT5-6 has roles other than binding to KMT2C/D.

Genetic interaction of PAXIP1 with the NIPBL-MAU2 cohesin loader complex

To characterize the genetic interactions of PAXIP1, we performed a genome-wide CRISPR screen in PAXIP1-KO cells. Among the 13 synthetically lethal hits at FDR < 0.1 were the cohesin factors STAG2, PDS5B and MAU2,

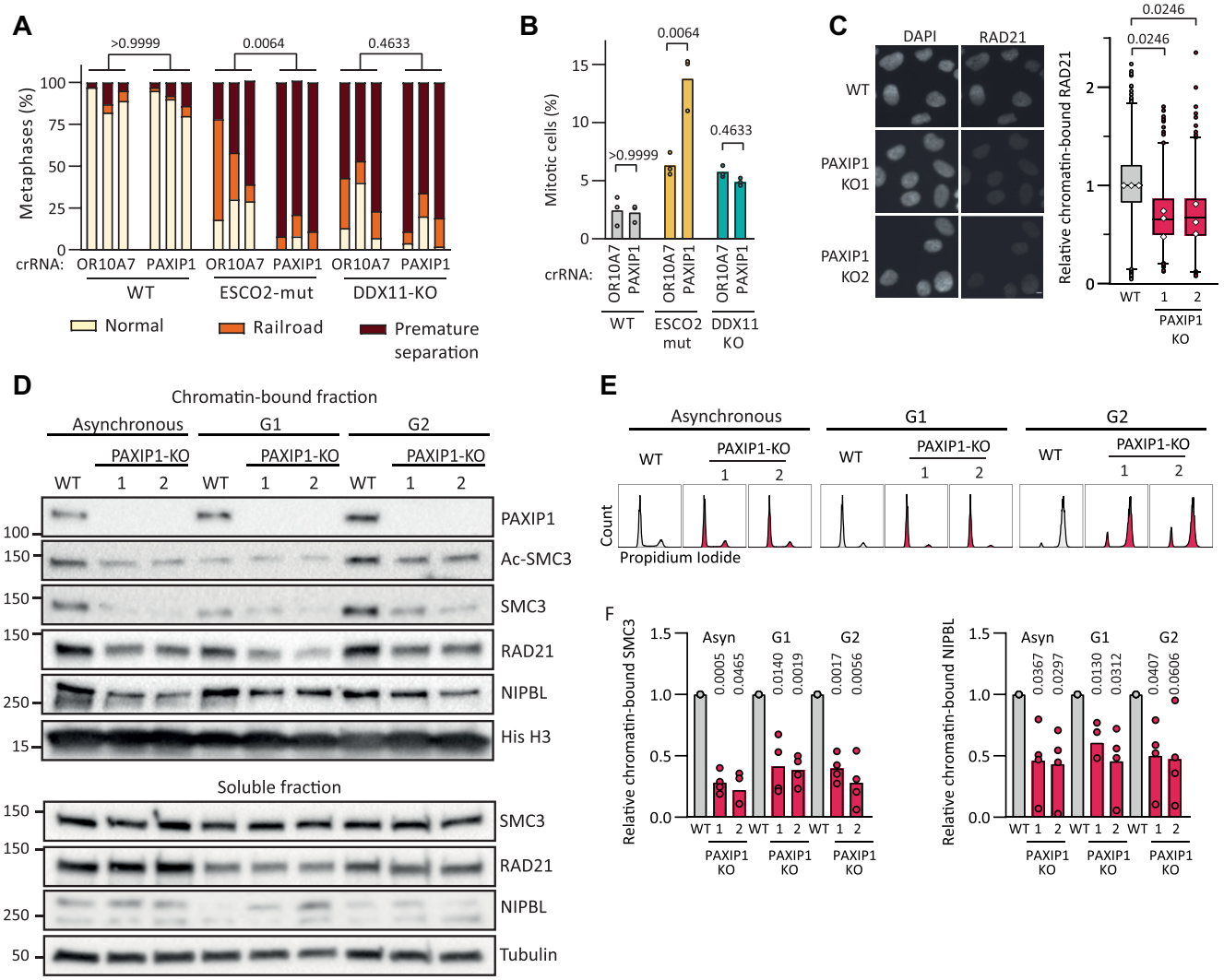

Figure 3. PAXIP1 promotes chromatin association of cohesin throughout the cell cycle. (**A**) Cohesion defect analysis two days after crPAXIP1 transfection. 50 metaphases were assessed for each sample, three independent experiments are shown as separate bars. *P*-values were calculated by a one-way ANOVA comparing the frequency of premature chromatid separation per condition. (**B**) Percentage of mitotic cells two days after crPAXIP1 transfection assessed by flow cytometry of p-histone H3-S10 stained cells from three independent experiments. P-values were calculated by a one-way ANOVA. (**C**) Chromatin-bound cohesin levels of WT, PAXIP1-KO1 and PAXIP1-KO2 cells assessed by RAD21 immunofluorescence of pre-extracted cells. RAD21 intensity was quantified for at least 205 cells per condition per experiment in three independent experiments. Box represents 25%-75% and median, whiskers represent 1–99 percentile from combined data points. *P*-values were calculated by a one-way ANOVA comparing the median values from separate biological replicates, which are indicated by white diamonds. Scale bar represents 5 μm. (**D**) Western blot of chromatin-bound and soluble protein fractions in WT and PAXIP1-KO cells in asynchronous cells (Asyn) or synchronized cells, in G1 by 10μM Palbociclib or in G2 by 10μM RO-3306. (**E**) Flow cytometry control of the synchronization in D. (**F**) Quantification of chromatin-bound SMC3 and NIPBL normalized to Histone H3 relative to WT from four independent experiments. P-values were calculated by one sample *T* tests against a null hypothesis of 1.

further implicating PAXIP1 in cohesin regulation (Figure 5A). Note that although ESCO2 depletion further reduced viability of PAXIP1-KO cells (Supplementary Figure S9A), ESCO2 was not detected as a hit in the CRISPR screen. This could relate to the critical role of ESCO2 in cellular proliferation in both PAXIP1-KO as well as WT cells or to crRNA specific effects. Intrigued by the identification of a synthetic lethal interaction between PAXIP1 and MAU2, we decided to further investigate the relationship between the cohesin loader complex NIPBL-MAU2 and PAXIP1. Transfection of crMAU2 or crNIPBL resulted in proliferation defects, particularly in PAXIP1-KO cells (Supplementary Figure S9A, B). PAXIP1 loss further aggravated the decrease in chromatin-bound cohesin upon depletion of MAU2 or NIPBL (Figure 5B-C). We then constructed stable MAU2-KO cells and subsequently made three MAU2-PAXIP1-dKO clones (Supplementary Figure S9C). MAU2 loss resulted in destabilization of NIPBL, in line with previous reports (69,70) (Figure 5D) and in slower proliferation compared to WT cells, which was further reduced in MAU2-PAXIP1-dKOs (Figure 5E). Furthermore, MAU2-KO cells had lower levels of chromatin-bound cohesin compared to WT and PAXIP1-KO cells, which were slightly further reduced in MAU2-PAXIP1-dKOs (Figure 5F).

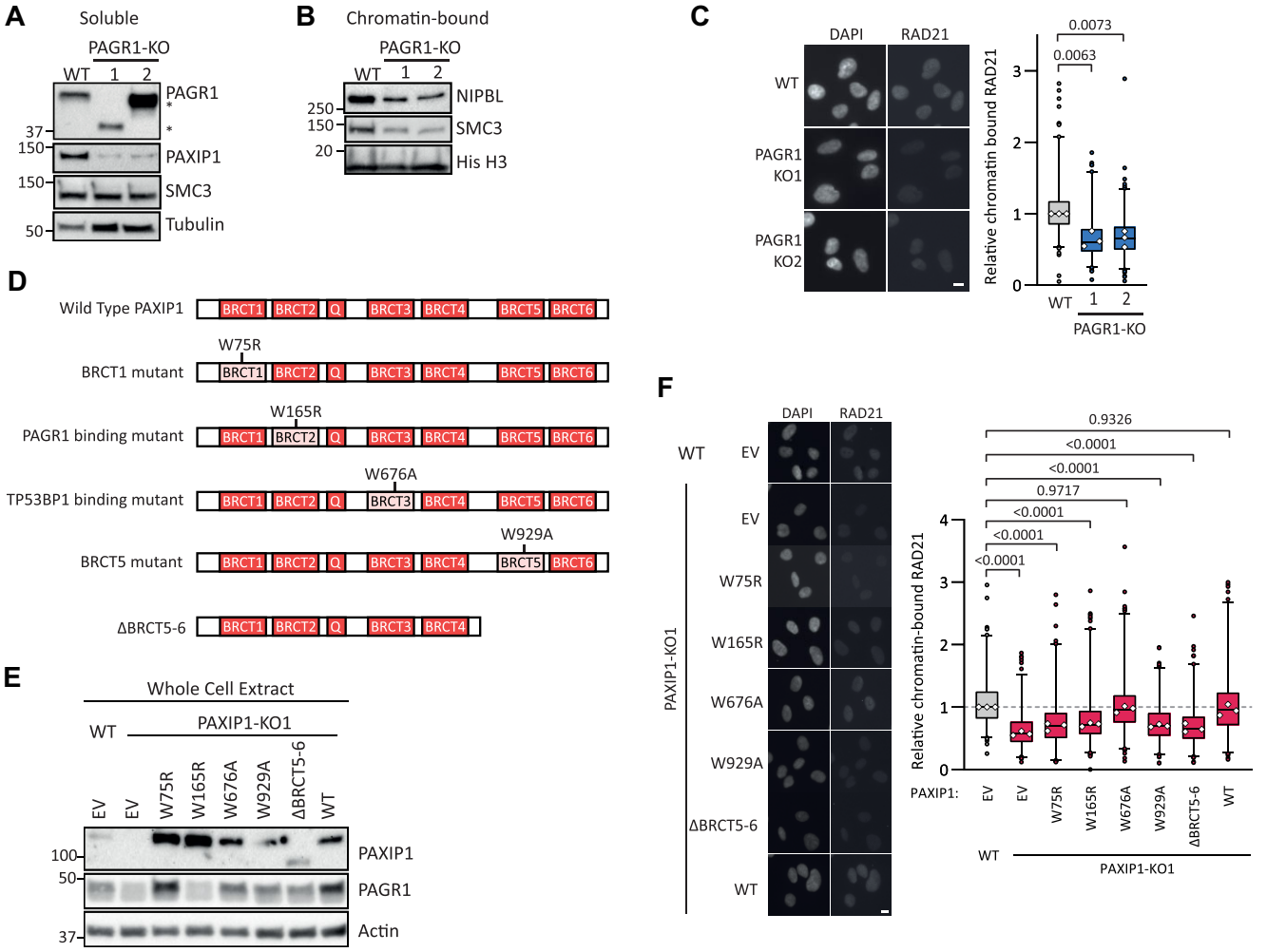

Figure 4. The role of PAXIP1 in maintaining chromatin-bound cohesin depends on the interaction with PAGR1. (**A**) Western blot of soluble protein fractions of WT and PAGR1-KOs cells. Asterisks indicate truncated proteins in PAGR1-KO clones, presumably resulting from a premature stop codon. (**B**) Western blot of chromatin bound protein fractions of WT and PAGR1-KO cells. (**C**) RAD21 immunofluorescence in pre-extracted PAGR1-KO cells. Intensity was quantified from three independent experiments with at least 155 cells per condition per experiment. Box represents 25–75% and median, whiskers represent 1–99 percentile from combined data points. *P*-values were calculated by a one-way ANOVA comparing the median values from separate biological replicates, which are indicated by white diamonds. Representative images are shown on the left. Scale bar represents 10 μm. (**D**) Schematic representation of PAXIP1 expression constructs (BRCT = BRCA1 C-terminus domain; Q = glutamine-rich domain). (**E**) Western blot of whole cell extract of WT and PAXIP1-KO cells, stably transduced with PAXIP1 constructs described in 4D. (**F**) RAD21 immunofluorescence in pre-extracted in PAXIP1 mutant cells. Intensity was quantified from three independent experiments with at least 105 cells per sample per experiment. Box represents 25–75% and median, whiskers represent 1–99 percentile from combined data points. *P*-values were calculated by a one-way ANOVA comparing the median values from separate biological replicates, which are indicated by white diamonds. Representative images are shown on the left. Scale bar represents 10 μm.

Possibly, PAXIP1 loss further diminishes the residual NIPBL-dependent cohesin loading activity in MAU2-KOs (69,70). Alternatively, rather than facilitating cohesin loading, these observations may point at a role for PAXIP1 in stabilizing cohesin on chromatin.

A conserved FDF motif in PAGR1 promotes cohesin occupancy on chromatin

Interestingly, we discovered that PAGR1 contains a FDFDD motif, which is conserved in vertebrates (Figure 6A). Similar F/YxF motifs (consensus [PFCAVIYL][FY][GDEN]F.(0,1)[DANE].(0,1)[DE]) have previously been found in several proteins, including CTCF, WAPL and MCM3, and were reported to mediate interactions at the STAG1/2-RAD21 interface and regulate cohesin dynamics on chromatin (29,71). Similar as described for CTCF (29), Alphafold2 predictions suggest that this FDF motif occurs in an unstructured region (Supplementary Figure S10A), and may interact with cohesin similarly as shown for CTCF (Supplementary Figure S10B). To test the relevance of this motif in PAGR1, we complemented PAGR1-KO1 with WT or mutant (ADA) FLAG-tagged PAGR1 (Figure 6B). Both WT and mutant PAGR1 could stabilize PAXIP1 and maintained interaction with PAXIP1 and chromatin (Figure 6B–D). However, unlike PAGR1-WT, the ADA mutant was unable to restore chromatin-bound cohesin levels (Figure 6C, E–F). While still in excess of endogenous levels, comparable results were found when using weaker expression of ectopic PAGR1

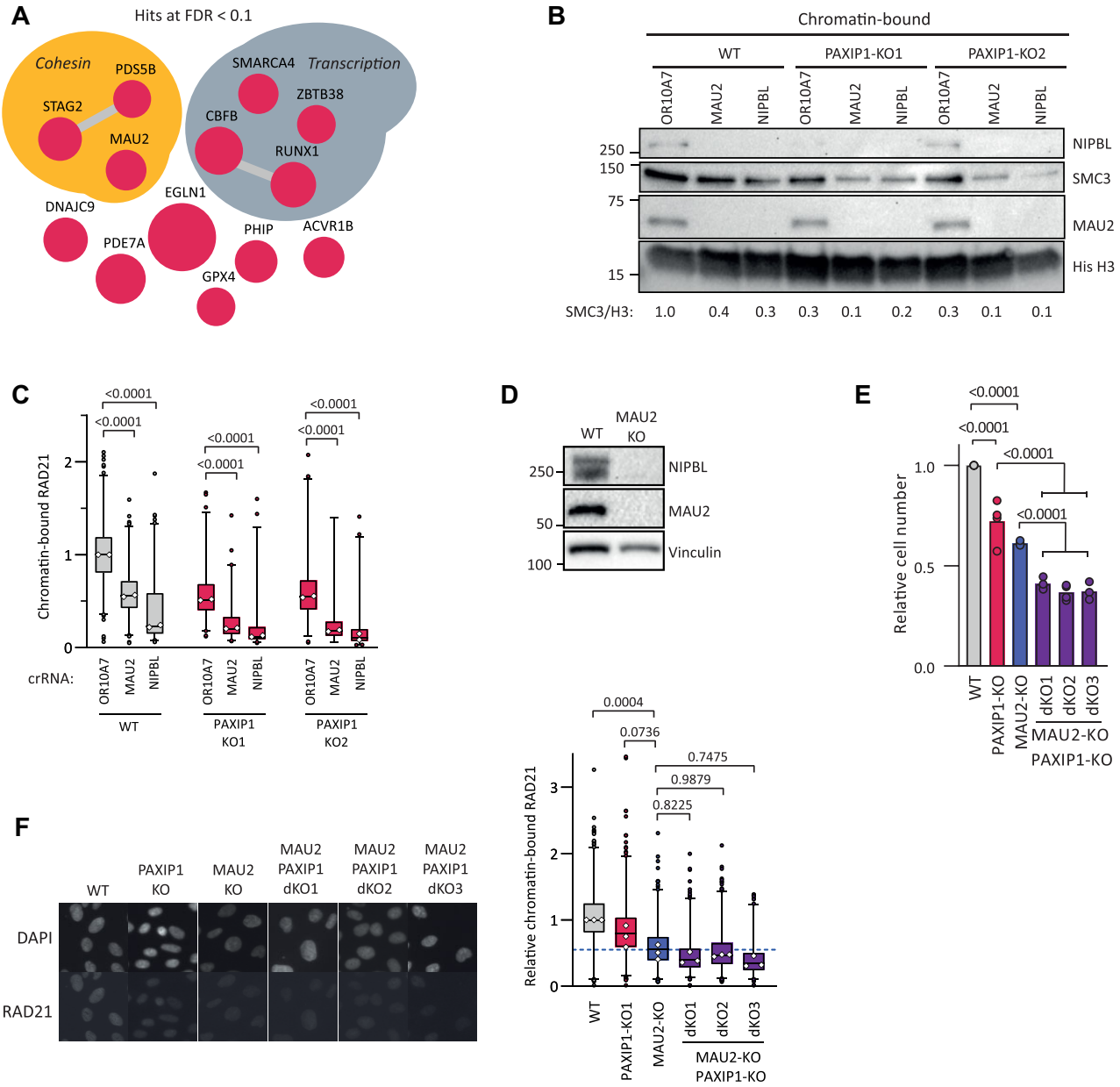

Figure 5. The genetic interaction between PAXIP1 and the cohesin loader NIPBL-MAU2. (**A**) Network of hits from a genome-wide CRISPR screen in PAXIP1-KO cells using FDR < 0.1. Edges indicate physical protein–protein interactions (String-db, evidence-based), node size reflects significance. Raw data in Supplementary Table S1. (**B**) Western blot of chromatin-bound protein fractions of WT and PAXIP1-KOs after transfection with indicated crRNAs. SMC3 band intensities were quantified using Image Lab relative to WT crOR10A7 levels, corrected for histone H3 and are depicted below the blot. (**C**) WT and PAXIP1-KO cells were transfected with indicated crRNAs and chromatin-bound cohesin was assessed by RAD21 immunofluorescence after pre-extraction. Intensity was quantified from two independent experiments with at least 88 cells per sample per experiment. Box represents 25–75% and median, whiskers represent 1–99 percentile from combined data points. *P*-values were calculated by a one-way ANOVA comparing the median values from separate biological replicates, which are indicated by white diamonds. (**D**) Western blot of whole cell extract from WT and MAU2-KO cells. (**E**) Cell counts relative to WT of indicated cells lines after four days proliferation. Dots represent the mean of two technical replicates; bars indicate the mean of four independent experiments. (**F**) Chromatin-bound cohesin assessed by RAD21 immunofluorescence after pre-extraction of PAXIP1-KO, MAU2-KO and PAXIP1-MAU2-doubleKO cell lines. At least 100 cells were scored per condition per experiment in three independent experiments. Box represents 25–75% and median, whiskers represent 1–99 percentile from combined data points. *P*-values were calculated by a one-way ANOVA comparing the median values from separate biological replicates, which are indicated by white diamonds. Representative images are shown on the left.

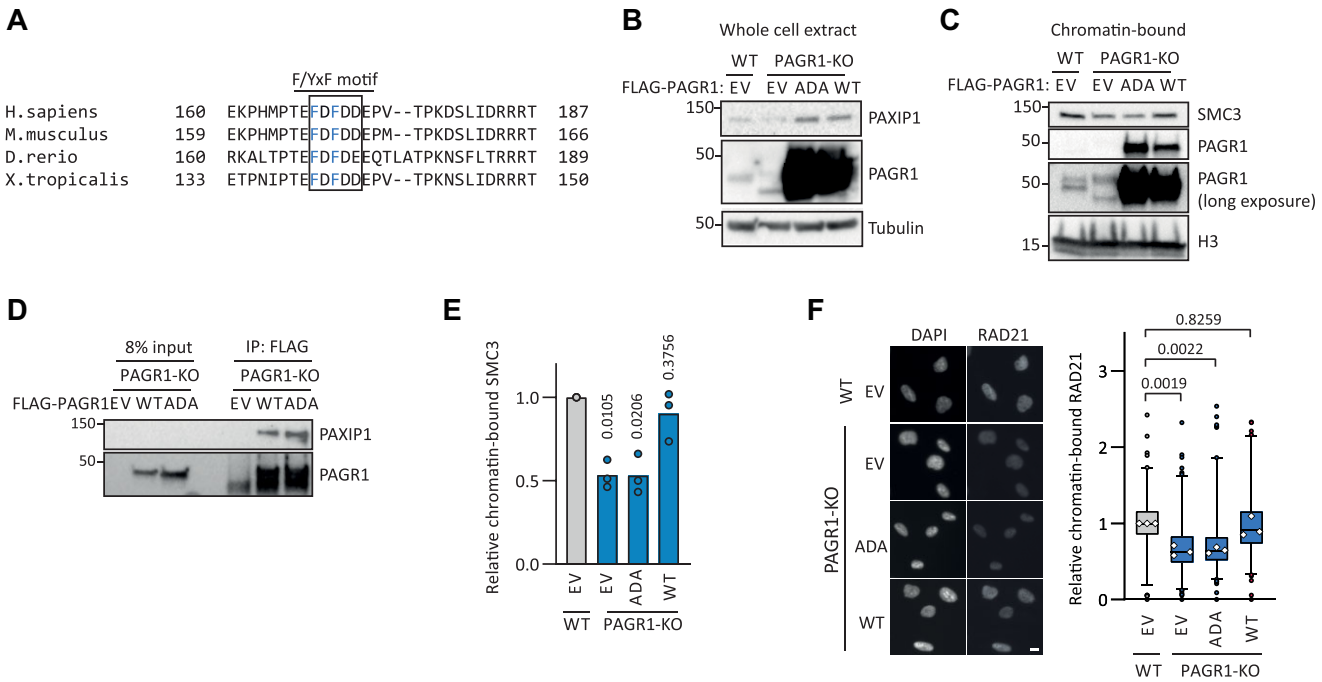

Figure 6. A conserved FDF motif in PAGR1 promotes cohesin occupancy on chromatin. (**A**) Sequence alignment of PAGR1 at the FDF motif. Box indicates the consensus FDFDD sequence, blue amino acids indicate phenylalanines mutated to alanines in the ADA mutant. (B, C) PAGR1-KO cells were stably transduced with empty vector (EV), FLAG-tagged WT or mutant (ADA) PAGR1. Whole cell extract (**B**) and chromatin-bound protein fractions (**C**) were assessed by western blot. (**D**) Flag-PAGR1 was immunoprecipitated from indicated cell lines followed by western blot analysis. (**E**) SMC3 band intensities were quantified from three independent western blots relative to WT-EV levels, corrected for Histone H3. P-values were calculated by one sample T tests against a null hypothesis of 1. (**F**) RAD21 intensity was quantified in indicated cell lines in three independent experiments with at least 142 cells per sample per experiment. Box represents 25%-75% and median, whiskers represent 1–99 percentile from combined data points. *P*-values were calculated by a one-way ANOVA comparing the median values from separate biological replicates, which are indicated by white diamonds. Scale bar represents 10 μm.

(Supplementary Figure S10C, D). In conclusion, cohesin occupancy on chromatin depends on the FDF motif in PAGR1.

PAXIP1 interacts and co-localizes with cohesin on chromatin at active promoters and enhancers

Since F/YxF motifs have been linked to cohesin binding (29), this may suggest PAXIP1-PAGR1 physically interacts with cohesin. In line, mass spectrometry of PAXIP1 co-precipitating proteins previously revealed SMC1 in HEK293T cells (65) and NIPBL in HeLa cells (72). Using co-immunoprecipitation experiments, we could indeed detect a physical interaction of Venus-tagged PAXIP1 with RAD21 in RPE1 cells (Supplementary Figure S11A, B). To assess the contribution of PAGR1 to the PAXIP1-cohesin interaction, we disrupted endogenous PAGR1 in the Venus-PAXIP1 expressing cell line (Supplementary Figure S11C). Similar as in Figure 4, we observed reduced RAD21 on DNA upon PAGR1 disruption (Figure 7A, first three lanes), indicating that the truncated PAGR1 protein product can no longer promote chromatin association of cohesin. We then introduced WT and mutant (ADA) PAGR1 and performed co-IP of Venus-PAXIP1. This revealed an interaction of PAXIP1 with RAD21 and MAU2, which was reduced upon PAGR1 disruption (Figure 7B). Whereas this could be restored by WT-PAGR1, the effect of mutant PAGR1 was less pronounced (Figure 7B). This indicates that PAGR1 facilitates the binding of PAXIP1 to cohesin, at least in part via its FDF motif.

To determine if PAXIP1 localizes to cohesin-bound genomic regions, we mined publicly available ChIP-seq data for the human hepatocellular carcinoma cell line HepG2 from ENCODE (73,74). This revealed that PAXIP1 occupied genomic sites that are enriched in RAD21 binding (Figure 7C). As expected, sites with the strongest RAD21 signal co-localized with CTCF (Figure 7D). Interestingly, PAXIP1 particularly occupied sites with a weaker CTCF signal (Figure 7D, E), suggesting that PAXIP1 and cohesin preferentially co-localize at genomic loci that are less frequently bound by CTCF. To identify the chromosomal sites at which PAXIP1 and RAD21 co-localize, we examined promoters and enhancers. Previous reports described localization of PAXIP1 to promoters (56,75). In line with this, we found that PAXIP1 is enriched at transcription start sites (TSSs) enriched for RNA Polymerase II (POLR2A) and H3K4me3, indicative of active promoters and co-localizes with RAD21 at these sites (Figure 7F). In addition, PAXIP1 and RAD21 co-localize at active enhancers, defined by enrichment of the histone acetyltransferase p300 and H3K4me1 (Supplementary Figure S12). Together, these data suggest that PAXIP1 co-localizes with cohesin at active promoters and enhancers.

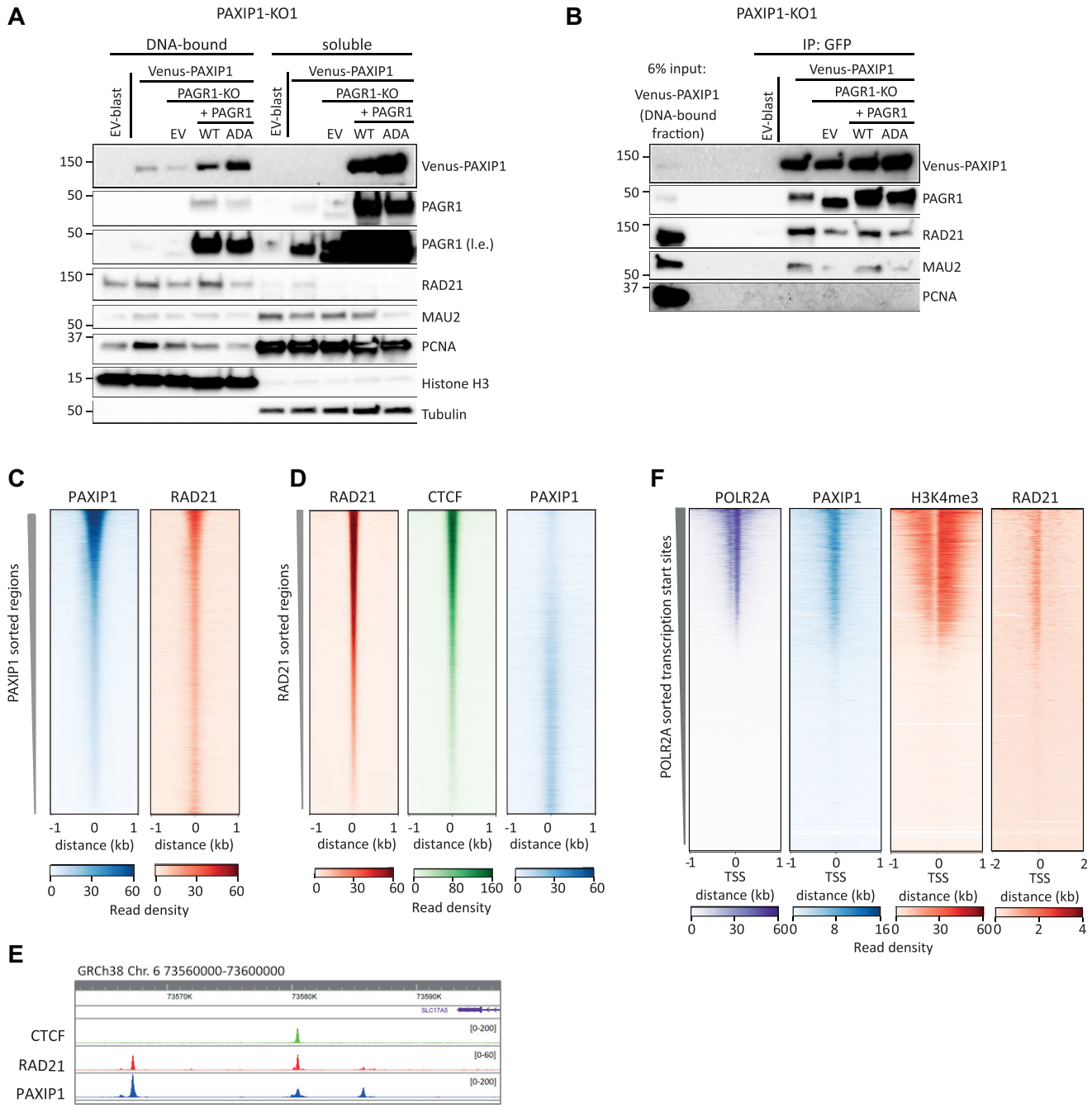

Figure 7. PAXIP1 interacts and co-localizes with cohesin on chromatin. (**A**) PAXIP1-KO1 RPE1 cells were stably transduced with empty vector (EV-blast) or Venus-PAXIP1, followed by disruption of endogenous PAGR1 and complementation with EV, WT or mutant (ADA) PAGR1. Chromatin-bound and soluble protein fractions were isolated and analyzed by western blot. (**B**) DNA-bound protein fractions from (A) were used for co- immunoprecipitation of Venus-PAXIP1 using GFP-trap beads, followed by western blot. (**C**) Heatmaps of ENCODE ChIP-seq data for HepG2 cells sorted on PAXIP1 enriched regions. Regions are centered on PAXIP1 peaks ±1 kb. (**D**) Heatmaps of ENCODE ChIP-seq data for HepG2 cells sorted on RAD21 enriched regions. Regions are centered on RAD21 peaks ±1 kb. **(E)** Genome browser screenshot of ChIP-seq signals for RAD21, CTCF and PAXIP1 in HepG2 cells. (**F**) Heatmaps of ENCODE ChIP-seq data for HepG2 cells sorted on transcription start sites (TSSs) enriched for POLR2A. Regions are centered on TSSs ±1 kb.

DISCUSSION

Here, we present a high-confidence network of genetic dependencies of DDX11 and ESCO2 deficient cells. This reveals multiple genes previously linked to sister chromatid cohesion that confirm the presence of parallel cohesion establishment pathways (11,12,24). In addition, we validated the microtubule motor protein DYNC1Li2 as one of many mitotic regulators that become particularly essential in a cohesion-compromised background, thus representing potential therapeutic targets for cohesion defective cancers (23). Confidence of the identified hits is further underscored by multiple previously described interactions with genes involved in the response to DNA damage and DNA replication stress. While we chose to further investigate the PAXIP1-PAGR1 complex, it will be interesting to experimentally follow up some of the other newly identified genetic interactions.

We find that PAXIP1-PAGR1 directly promotes the chromatin association of cohesin. Our analysis of ENCODE ChIP-seq data suggests that PAXIP1 particularly co-localizes with cohesin on sites that are not bound by CTCF. While CTCF-bound cohesin sites are mostly similar in different tissues, non-CTCF binding cohesin often localizes to cell-type specific transcription factors and active enhancers in specific genomic regions, frequently associated with cell identity genes (76–79). Since PAXIP1 binding is also enriched at promoters and enhancers and is necessary for long-range enhancer-promotor contacts (56,75,80), a function that is shared with cohesin (37,81,82), PAXIP1 may facilitate enhancer-promotor contacts by cohesin mediated loop formation. In line with this model, cohesin binding to glucocorticoid receptor (GR) binding sites depends on PAXIP1, resulting in a joint regulation of hormone-induced transcriptional activity via chromosome folding, described in the accompanying paper (83). Together, a picture emerges in which PAXIP1 facilitates chromatin binding of cohesin to regulate enhancer-promoter interactions, to control cell-type specific and context-responsive gene expression patterns.

Several mechanisms may explain how PAXIP1 promotes the chromatin association of cohesin. Cohesin and the cohesin loader co-precipitated with PAXIP1, similar as in other cellular models (65,72). Notably, these interactions were difficult to detect, possibly indicating that they are weak, transient and/or context-dependent. Thus, PAXIP1-PAGR1 may act as a direct chromatin acceptor for the cohesin loading reaction, as has been suggested for several other chromatin binding proteins (30,31,36,84–86), or stabilize cohesin on chromatin. This is further supported by FRAP analysis of SMC1-EGFP, which revealed reduced cohesin stability on chromatin in PAXIP1-KO cells (83). This may involve the FDF motif that we identified in PAGR1, which may antagonize WAPL similar as has been shown for CTCF (29) and MCM3 (71). The observation that PAXIP1 co-localizes with cohesin mainly at sites with no detected CTCF occupancy could be consistent with the fact that cohesin can only bind one F/YxF motif at a time (29). Alternatively, and not mutually exclusive, PAXIP1 may modulate chromatin to create an environment that promotes cohesin loading, for example by creating a nucleosome free template (30). Note that our ChIP-qPCR results show that in PAXIP1-KO cells, RAD21 binding is also reduced at CTCF binding sites (Supplementary Figure S5). Speculatively, PAXIP1 depletion may lead to reduced cohesin loading and/or impaired cohesin mobility (through decreased NIPBL levels on chromatin), that ultimately affects the amount of cohesin that accumulates at CTCF sites. Thus, PAXIP1-PAGR1 may promote recruitment and/or stabilization of cohesin onto chromatin, resulting in local cohesin enrichment.

PAXIP1 and PAGR1 are components of KMT2C/D H3K4 methyltransferase complexes, but also function as an independent sub-complex at multiple genomic loci (57). Our findings suggest that human KMT2C and KMT2D are not involved in promoting cohesin occupancy on chromatin. However, since we were unable to detect the proteins by western blot, we cannot exclude that incomplete depletions preclude a detectable effect. Of note, PAXIP1 functions together with cohesin in glucocorticoid receptor activity apparently independent from KMT2C/D (83), indeed pointing at a function of PAXIP1-PAGR1 separate from KMT2C/D in cohesin regulation. Nevertheless, two PAXIP1 mutants previously described to abrogate KMT2C/D binding (57,66) were unable to restore chromatin-bound cohesin, suggesting that BRCT5-6 has roles other than KMT2C/D binding.

In addition to regulating gene transcription, PAXIP1 has been implicated in immunoglobulin class switching and V(D)J recombination in B cells and in T cell receptor recombination (56,57,75), processes that also depend on chromatin looping and cohesin (80,87–90). Moreover, like cohesin, PAXIP1 localizes to DNA damage sites (66,91–94) and PAXIP1 has been shown to be important for downstream cohesin functions at DSBs (59). Considering the apparent overlap of processes that are controlled by PAXIP1 and cohesin, it will be interesting to determine to what extent these processes involve a direct effect of PAXIP1 on cohesin. Notably, hints that PAXIP1/PAGR1 interacts genetically with STAG2 have been found before (95,96), but the nature of this interaction (suppressor or sensitizer) seems to be context-dependent. What factors determine these differential outcomes remain to be investigated.

Although PAXIP1 is a hit in both screens, the effects of PAXIP1 loss are particularly pronounced in ESCO2 mutant cells, which may be related to the different functions of DDX11 and ESCO2 in cohesion establishment. Possibly, PAXIP1-dependent chromatin-bound cohesin complexes in G1 are converted to cohesive cohesin in S-phase, which would place PAXIP1 in the cohesin conversion pathway like DDX11 (13). Alternatively, since PAXIP1 was also shown to localize to the replication fork (97), it may assist in cohesion establishment directly at the fork. However, while we initially identified PAXIP1 for its function in sister chromatid cohesion in ESCO2-mut cells, PAXIP1-KO cells do not harbor cohesion defects. This is reminiscent of ESCO1 depletion which does not cause pronounced cohesion defects, except in the context of ESCO2 loss (14,16,50). Similar to PAXIP1 loss, a reduction of functional MAU2 or NIPBL reduces chromatin-bound cohesin but does not cause pronounced sister chromatid cohesion defects. Together our data suggest that PAXIP1 promotes multiple

cohesin regulatory functions by increasing the association of cohesin to chromatin.

DATA AVAILABILITY

RNA-seq data are deposited at the National Center for Biotechnology Information (NCBI) Gene Expression Omnibus (GEO), accession number GSE211349. The datasets of ChIP-seq experiments analyzed in this study are from ENCODE, details are provided in the Methods section.

SUPPLEMENTARY DATA

Supplementary Data are available at NAR Online.

ACKNOWLEDGEMENTS

We thank Isabel Mayayo-Peralta, Stefan Prekovic and Wilbert Zwart for sharing unpublished work and for insightful discussions, the Amsterdam UMC Core Facility Genomics for sequencing, the ENCODE Consortium and the Bernstein (Broad) and Myers (HAIB) lab for generating ENCODE datasets, and Yiping He for sharing HCT116 KMT2D-KO cells.

FUNDING

Dutch Cancer Society [KWF grants 10701 and 13645 to J.d.L.]. Funding for open access charge: Dedicated budget that is available within our own research group.
Conflict of interest statement. None declared.

This paper is linked to: doi:10.1093/nar/gkad267.

REFERENCES

1. Haarhuis,J.H., Elbatsh,A.M. and Rowland,B.D. (2014) Cohesin and its regulation: on the logic of X-shaped chromosomes. *Dev. Cell.*, **31**, 7–18.
2. Davidson,I.F. and Peters,J.M. (2021) Genome folding through loop extrusion by SMC complexes. *Nat. Rev. Mol. Cell Biol.*, **22**, 445–464.
3. Higashi,T.L., Pobegalov,G., Tang,M., Molodtsov,M.I. and Uhlmann,F. (2021) A Brownian ratchet model for DNA loop extrusion by the cohesin complex. *Elife*, **10**, e67530.
4. Waldman,T. (2020) Emerging themes in cohesin cancer biology. *Nat. Rev. Cancer*, **20**, 504–515.
5. Piché,J., Van Vliet,P.P., Pucéat,M. and Andelfinger,G. (2019) The expanding phenotypes of cohesinopathies: one ring to rule them all!. *Cell Cycle*, **18**, 2828–2848.
6. van Schie,J.J.M. and de Lange,J. (2021) The interplay of cohesin and the replisome at processive and stressed DNA replication forks. *Cells*, **10**, 3455.
7. Bender,D., Da Silva,E.M.L., Chen,J., Poss,A., Gawey,L., Rulon,Z. and Rankin,S. (2020) Multivalent interaction of ESCO2 with the replication machinery is required for sister chromatid cohesion in vertebrates. *Proc. Natl. Acad. Sci. U.S.A.*, **117**, 1081–1089.
8. Rankin,S., Ayad,N.G. and Kirschner,M.W. (2005) Sororin, a substrate of the anaphase- promoting complex, is required for sister chromatid cohesion in vertebrates. *Mol. Cell*, **18**, 185–200.
9. Ladurner,R., Kreidl,E., Ivanov,M.P., Ekker,H., Idarraga-Amado,M.H., Busslinger,G.A., Wutz,G., Cisneros,D.A. and Peters,J.M. (2016) Sororin actively maintains sister chromatid cohesion. *EMBO J.*, **35**, 635–653.
10. Nishiyama,T., Ladurner,R., Schmitz,J., Kreidl,E., Schleiffer,A., Bhaskara,V., Bando,M., Shirahige,K., Hyman,A.A., Mechtler,K. *et al.* (2010) Sororin mediates sister chromatid cohesion by antagonizing Wapl. *Cell*, **143**, 737–749.
11. Borges,V., Smith,D.J., Whitehouse,I. and Uhlmann,F. (2013) An Eco1-independent sister chromatid cohesion establishment pathway in S. cerevisiae. *Chromosoma*, **122**, 121–134.
12. Xu,H., Boone,C. and Brown,G.W. (2007) Genetic dissection of parallel sister-chromatid cohesion pathways. *Genetics*, **176**, 1417–1429.
13. Srinivasan,M., Fumasoni,M., Petela,N.J., Murray,A. and Nasmyth,K.A. (2020) Cohesion is established during DNA replication utilising chromosome associated cohesin rings as well as those loaded de novo onto nascent dnas. *Elife*, **9**, e56611.
14. Faramarz,A., Balk,J.A., van Schie,J.J.M., Oostra,A.B., Ghandour,C.A., Rooimans,M.A., Wolthuis,R.M.F. and de Lange,J. (2020) Non-redundant roles in sister chromatid cohesion of the DNA helicase DDX11 and the SMC3 acetyl transferases ESCO1 and ESCO2. *PLoS One*, **15**, e0220348.
15. Abe,T., Kawasumi,R., Arakawa,H., Hori,T., Shirahige,K., Losada,A., Fukagawa,T. and Branzei,D. (2016) Chromatin determinants of the inner-centromere rely on replication factors with functions that impart cohesion. *Oncotarget*, **7**, 67934–67947.
16. Kawasumi,R., Abe,T., Arakawa,H., Garre,M., Hirota,K. and Branzei,D. (2017) ESCO1/2's roles in chromosome structure and interphase chromatin organization. *Genes Dev.*, **31**, 2136–2150.
17. Kukolj,E., Kaufmann,T., Dick,A.E., Zeillinger,R., Gerlich,D.W. and Slade,D. (2017) PARP inhibition causes premature loss of cohesion in cancer cells. *Oncotarget*, **8**, 103931–103951.
18. Jegadesan,N.K. and Branzei,D. (2021) DDX11 loss causes replication stress and pharmacologically exploitable DNA repair defects. *Proc. Natl. Acad. Sci. U.S.A.*, **118**, e2024258118.
19. Olivieri,M., Cho,T., Álvarez-Quilón,A., Li,K., Schellenberg,M.J., Zimmermann,M., Hustedt,N., Rossi,S.E., Adam,S., Melo,H. *et al.* (2020) A genetic map of the response to DNA damage in human cells. *Cell*, **182**, 481–496.
20. van Schie,J.J.M., Faramarz,A., Balk,J.A., Stewart,G.S., Cantelli,E., Oostra,A.B., Rooimans,M.A., Parish,J.L., de Almeida Estéves,C., Dumic,K. *et al.* (2020) Warsaw Breakage Syndrome associated DDX11 helicase resolves G-quadruplex structures to support sister chromatid cohesion. *Nat. Commun.*, **11**, 4287.
21. McLellan,J.L., O'Neil,N.J., Barrett,I., Ferree,E., van Pel,D.M., Ushey,K., Sipahimalani,P., Bryan,J., Rose,A.M. and Hieter,P. (2012) Synthetic lethality of cohesins with PARPs and replication fork mediators. *PLoS Genet.*, **8**, e1002574.
22. Benedict,B., Van Schie,J.J.M., Oostra,A.B., Balk,J.A., Wolthuis,R.M.F., Te Riele,H. and De Lange,J. (2020) WAPL-dependent repair of damaged DNA replication forks underlies oncogene-induced loss of sister chromatid cohesion. *Dev. Cell*, **52**, 683–698.
23. De Lange,J., Faramarz,A., Oostra,A.B., De Menezes,R.X., Van Der Meulen,I.H., Rooimans,M.A., Rockx,D.A., Brakenhoff,R.H., Van Beusechem,V.W., King,R.W. *et al.* (2015) Defective sister chromatid cohesion is synthetically lethal with impaired APC/C function. *Nat. Commun.*, **6**, 8399.
24. Kawasumi,R., Abe,T., Psakhye,I., Miyata,K., Hirota,K. and Branzei,D. (2021) Vertebrate CTF18 and DDX11 essential function in cohesion is bypassed by preventing WAPL-mediated cohesin release. *Genes Dev.*, **35**, 1368–1382.
25. Heidinger-Pauli,J.M., Mert,O., Davenport,C., Guacci,V. and Koshland,D. (2010) Systematic reduction of cohesin differentially affects chromosome segregation, condensation, and DNA repair. *Curr. Biol.*, **20**, 957–963.
26. Carvalhal,S., Tavares,A., Santos,M.B., Mirkovic,M. and Oliveira,R.A. (2018) A quantitative analysis of cohesin decay in mitotic fidelity. *J. Cell Biol.*, **217**, 3343–3353.
27. Davidson,I.F., Bauer,B., Goetz,D., Tang,W., Wutz,G. and Peters,J.M. (2019) DNA loop extrusion by human cohesin. *Science*, **366**, 1338–1345.
28. Kim,Y., Shi,Z., Zhang,H., Finkelstein,I.J. and Yu,H. (2019) Human cohesin compacts DNA by loop extrusion. *Science*, **366**, 1345–1349.
29. Li,Y., Haarhuis,J.H.I., Sedeno Cacciatore,A., Oldenkamp,R., van Ruiten,M.S., Willems,L., Teunissen,H., Muir,K.W., de Wit,E., Rowland,B.D. *et al.* (2020) The structural basis for cohesin-CTCF-anchored loops. *Nature*, **578**, 472–476.
30. Muñoz,S., Minamino,M., Casas-Delucchi,C.S., Patel,H. and Uhlmann,F. (2019) A role for chromatin remodeling in cohesin loading onto chromosomes. *Mol. Cell*, **74**, 664–673.

31. Zheng,G., Kanchwala,M., Xing,C. and Yu,H. (2018) MCM2–7-dependent cohesin loading during S phase promotes sister-chromatid cohesion. *Elife*, **7**, e33920.
32. Takahashi,T.S., Yiu,P., Chou,M.F., Gygi,S. and Walter,J.C. (2004) Recruitment of Xenopus Scc2 and cohesin to chromatin requires the pre-replication complex. *Nat. Cell Biol.*, **6**, 991–996.
33. Hinshaw,S.M., Makrantoni,V., Harrison,S.C. and Marston,A.L. (2017) The kinetochore receptor for the cohesin loading complex. *Cell*, **171**, 72–84.
34. Olley,G., Ansari,M., Bengani,H., Grimes,G.R., Rhodes,J., von Kriegsheim,A., Blatnik,A., Stewart,F.J., Wakeling,E., Carroll,N. *et al.* (2018) BRD4 interacts with NIPBL and BRD4 is mutated in a Cornelia de Lange-like syndrome. *Nat. Genet.*, **50**, 329–332.
35. Garcia-Luis,J., Lazar-Stefanita,L., Gutierrez-Escribano,P., Thierry,A., Cournac,A., García,A., González,S., Sánchez,M., Jarmuz,A., Montoya,A. *et al.* (2019) FACT mediates cohesin function on chromatin. *Nat. Struct. Mol. Biol.*, **26**, 970–979.
36. Hakimi,M.A., Bochar,D.A., Schmiesing,J.A., Dong,Y., Barak,O.G., Spelcher,D.W., Yokomori,K. and Shiekhattar,R. (2002) A chromatin remodelling complex that loads cohesin onto human chromosomes. *Nature*, **418**, 994–998.
37. Kagey,M.H., Newman,J.J., Bilodeau,S., Zhan,Y., Orlando,D.A., Van Berkum,N.L., Ebmeier,C.C., Goossens,J., Rahl,P.B., Levine,S.S. *et al.* (2010) Mediator and cohesin connect gene expression and chromatin architecture. *Nature*, **467**, 430–435.
38. van der Weegen,Y., de Lint,K., van den Heuvel,D., Nakazawa,Y., Mevissen,T.E.T., van Schie,J.J.M., San Martin Alonso,M., Boer,D.E.C., Gonzalez-Prieto,R., Narayanan,I.V. *et al.* (2021) ELOF1 is a transcription-coupled DNA repair factor that directs RNA polymerase II ubiquitylation. *Nat. Cell Biol.*, **23**, 595–607.
39. Guo,C., Chang,C.C., Wortham,M., Chen,L.H., Kernagis,D.N., Qin,X., Cho,Y.W., Chi,J.T., Grant,G.A., McLendon,R.E. *et al.* (2012) Global identification of MLL2-targeted loci reveals MLL2's role in diverse signaling pathways. *Proc. Natl. Acad. Sci. U.S.A.*, **109**, 17603–17608.
40. Conant,D., Hsiau,T., Rossi,N., Oki,J., Maures,T., Waite,K., Yang,J., Joshi,S., Kelso,R., Holden,K. *et al.* (2022) Inference of CRISPR Edits from Sanger Trace Data. *CRISPR J*, **5**, 123–130.
41. Hart,T., Tong,A.H.Y., Chan,K., Van Leeuwen,J., Seetharaman,A., Aregger,M., Chandrashekhar,M., Hustedt,N., Seth,S., Noonan,A. *et al.* (2017) Evaluation and Design of Genome-Wide CRISPR/SpCas9 Knockout Screens. *G3 (Bethesda)*, **7**, 2719–2727.
42. van Schie,J.J., de Lint,K., Pai,G.M., Rooimans,M.A., Wolthuis,R.M. and de Lange,J. (2023) MMS22L-TONSL functions in sister chromatid cohesion in a pathway parallel to DSCC1-RFC. *Life Sci. Alliance*, **6**, e202201596.
43. Moronta Gines,M. and Wendt,K.S. (2022) A Robust Protocol for Investigating the Cohesin Complex by ChIP-Sequencing. *Methods Mol. Biol.*, **2458**, 113–122.
44. Chen,S., Zhou,Y., Chen,Y. and Gu,J. (2018) fastp: an ultra-fast all-in-one FASTQ preprocessor. *Bioinformatics*, **34**, i884–i890.
45. Kim,D., Paggi,J.M., Park,C., Bennett,C. and Salzberg,S.L. (2019) Graph-based genome alignment and genotyping with HISAT2 and HISAT-genotype. *Nat. Biotechnol.*, **37**, 907–915.
46. 1000 Genome Project Data Processing Subgroup, Li,H., Handsaker,B., Wysoker,A., Fennell,T., Ruan,J., Homer,N., Marth,G., Abecasis,G. and Durbin,R. (2009) The Sequence Alignment/Map format and SAMtools. *Bioinformatics*, **25**, 2078–2079.
47. Liao,Y., Smyth,G.K. and Shi,W. (2014) featureCounts: an efficient general purpose program for assigning sequence reads to genomic features. *Bioinformatics*, **30**, 923–930.
48. Robinson,M.D., McCarthy,D.J. and Smyth,G.K. (2010) edgeR: a Bioconductor package for differential expression analysis of digital gene expression data. *Bioinformatics*, **26**, 139–140.
49. Ramirez,F., Ryan,D.P., Gruning,B., Bhardwaj,V., Kilpert,F., Richter,A.S., Heyne,S., Dundar,F. and Manke,T. (2016) deepTools2: a next generation web server for deep-sequencing data analysis. *Nucleic Acids Res.*, **44**, W160–W165.
50. Alomer,R.M., da Silva,E.M.L., Chen,J., Piekarz,K.M., McDonald,K., Sansam,C.G., Sansam,C.L. and Rankin,S. (2017) Esco1 and Esco2 regulate distinct cohesin functions during cell cycle progression. *Proc. Natl. Acad. Sci. U.S.A.*, **114**, 9906–9911.
51. Ivanov,M.P., Ladurner,R., Poser,I., Beveridge,R., Rampler,E., Hudecz,O., Novatchkova,M., Hériché,J.K., Wutz,G., van der Lelij,P. *et al.* (2018) The replicative helicase MCM recruits cohesin acetyltransferase ESCO2 to mediate centromeric sister chromatid cohesion. *EMBO J.*, **37**, e97150.
52. Minamino,M., Tei,S., Negishi,L., Kanemaki,M.T., Yoshimura,A., Sutani,T., Bando,M. and Shirahige,K. (2018) Temporal regulation of ESCO2 degradation by the MCM complex, the CUL4-DDB1-VPRBP complex, and the anaphase-promoting complex. *Curr. Biol.*, **28**, 2665–2672.
53. Mair,B., Tomic,J., Masud,S.N., Tonge,P., Weiss,A., Usaj,M., Tong,A.H.Y., Kwan,J.J., Brown,K.R., Titus,E. *et al.* (2019) Essential gene profiles for human pluripotent stem cells identify uncharacterized genes and substrate dependencies. *Cell Rep.*, **27**, 599–615.
54. Colic,M., Wang,G., Zimmermann,M., Mascall,K., McLaughlin,M., Bertolet,L., Lenoir,W.F., Moffat,J., Angers,S., Durocher,D. *et al.* (2019) Identifying chemogenetic interactions from CRISPR screens with drugZ. *Genome Med.*, **11**, 52.
55. Abe,T., Ooka,M., Kawasumi,R., Miyata,K., Takata,M., Hirota,K. and Branzei,D. (2018) Warsaw breakage syndrome DDX11 helicase acts jointly with RAD17 in the repair of bulky lesions and replication through abasic sites. *Proc. Nat. Acad. Sci. U.S.A.*, **115**, 8412–8417.
56. Daniel,J.A., Santos,M.A., Wang,Z., Zang,C., Schwab,K.R., Jankovic,M., Filsuf,D., Chen,H.T., Gazumyan,A., Yamane,A. *et al.* (2010) PTIP promotes chromatin changes critical for immunoglobulin class switch recombination. *Science*, **329**, 917–923.
57. Starnes,L.M., Su,D., Pikkupeura,L.M., Weinert,B.T., Santos,M.A., Mund,A., Soria,R., Cho,Y.W., Pozdnyakova,I., Højfeldt,M.K. *et al.* (2016) A PTIP-PA1 subcomplex promotes transcription for IgH class switching independently from the associated MLL3/MLL4 methyltransferase complex. *Genes Dev.*, **30**, 149–163.
58. Munoz,I.M., Jowsey,P.A., Toth,R. and Rouse,J. (2007) Phospho-epitope binding by the BRCT domains of hPTIP controls multiple aspects of the cellular response to DNA damage. *Nucleic Acids Res.*, **35**, 5312–5322.
59. Wu,J., Prindle,M.J., Dressler,G.R. and Yu,X. (2009) PTIP regulates 53BP1 and SMC1 at the DNA damage sites. *J. Biol. Chem.*, **284**, 18078–18084.
60. Wang,J., Aroumougame,A., Lobrich,M., Li,Y., Chen,D., Chen,J. and Gong,Z. (2014) PTIP associates with Artemis to dictate DNA repair pathway choice. *Genes Dev.*, **28**, 2693–2698.
61. Wang,X., Takenaka,K. and Takeda,S. (2010) PTIP promotes DNA double-strand break repair through homologous recombination. *Genes Cells*, **15**, 243–254.
62. Castedo,M., Perfettini,J.L., Roumier,T., Andreau,K., Medema,R. and Kroemer,G. (2004) Cell death by mitotic catastrophe: a molecular definition. *Oncogene*, **23**, 2825–2837.
63. Kim,E., Dede,M., Lenoir,W.F., Wang,G., Srinivasan,S., Colic,M. and Hart,T. (2019) A network of human functional gene interactions from knockout fitness screens in cancer cells. *Life Sci. Alliance*, **2**, e201800278.
64. Cho,Y.W., Hong,T., Hong,S.H., Guo,H., Yu,H., Kim,D., Guszczynski,T., Dressler,G.R., Copeland,T.D., Kalkum,M. *et al.* (2007) PTIP associates with MLL3- and MLL4-containing histone H3 lysine 4 methyltransferase complex. *J. Biol. Chem.*, **282**, 20395–20406.
65. Patel,S.R., Kim,D., Levitan,I. and Dressler,G.R. (2007) The BRCT-domain containing protein PTIP links PAX2 to a histone H3, lysine 4 methyltransferase complex. *Dev. Cell*, **13**, 580–592.
66. Gong,Z., Cho,Y.W., Kim,J.E., Ge,K. and Chen,J. (2009) Accumulation of pax2 transactivation domain interaction protein (PTIP) at sites of DNA breaks via RNF8-dependent pathway is required for cell survival after DNA damage. *J. Biol. Chem.*, **284**, 7284–7293.
67. Lavery,W.J., Barski,A., Wiley,S., Schorry,E.K. and Lindsley,A.W. (2020) KMT2C/D COMPASS complex-associated diseases [KCDCOM-ADs]: an emerging class of congenital regulopathies. *Clin. Epigenetics*, **12**, 10.
68. Watanabe,Y., Castoro,R.J., Kim,H.S., North,B., Oikawa,R., Hiraishi,T., Ahmed,S.S., Chung,W., Cho,M.Y., Toyota,M. *et al.* (2011) Frequent alteration of MLL3 frameshift mutations in microsatellite deficient colorectal cancer. *PLoS One*, **6**, e23320.
69. Parenti,I., Diab,F., Gil,S.R., Mulugeta,E., Casa,V., Berutti,R., Brouwer,R.W.W., Dupé,V., Eckhold,J., Graf,E. *et al.* (2020) MAU2 and NIPBL variants impair the heterodimerization of the cohesin

loader subunits and cause cornelia de Lange Syndrome. *Cell Rep.*, **31**, 107647
70. Haarhuis,J.H.I., van der Weide,R.H., Blomen,V.A., Yáñez-Cuna,J.O., Amendola,M., van Ruiten,M.S., Krijger,P.H.L., Teunissen,H., Medema,R.H., van Steensel,B. *et al.* (2017) The cohesin release factor WAPL restricts chromatin loop extension. *Cell*, **169**, 693–707.
71. Dequeker,B.J.H., Scherr,M.J., Brandao,H.B., Gassler,J., Powell,S., Gaspar,I., Flyamer,I.M., Lalic,A., Tang,W., Stocsits,R. *et al.* (2022) MCM complexes are barriers that restrict cohesin-mediated loop extrusion. *Nature*, **606**, 197–203.
72. van Nuland,R., Smits,A.H., Pallaki,P., Jansen,P.W.T.C., Vermeulen,M. and Timmers,H.T.M. (2013) Quantitative dissection and stoichiometry determination of the human SET1/MLL histone methyltransferase complexes. *Mol. Cell. Biol.*, **33**, 2067–2077.
73. The ENCODE Project Consortium (2012) An integrated encyclopedia of DNA elements in the human genome. *Nature*, **489**, 57–74.
74. Luo,Y., Hitz,B.C., Gabdank,I., Hilton,J.A., Kagda,M.S., Lam,B., Myers,Z., Sud,P., Jou,J., Lin,K. *et al.* (2020) New developments on the Encyclopedia of DNA Elements (ENCODE) data portal. *Nucleic Acids Res.*, **48**, D882–D889.
75. Callen,E., Faryabi,R.B., Luckey,M., Hao,B., Daniel,J.A., Yang,W., Sun,H.W., Dressler,G., Peng,W., Chi,H. *et al.* (2012) The DNA damage- and transcription-associated protein Paxip1 controls thymocyte development and emigration. *Immunity*, **37**, 971–985.
76. Faure,A.J., Schmidt,D., Watt,S., Schwalie,P.C., Wilson,M.D., Xu,H., Ramsay,R.G., Odom,D.T. and Flicek,P. (2012) Cohesin regulates tissue-specific expression by stabilizing highly occupied cis-regulatory modules. *Genome Res.*, **22**, 2163–2175.
77. Nitzsche,A., Paszkowski-Rogacz,M., Matarese,F., Janssen-Megens,E.M., Hubner,N.C., Schulz,H., de Vries,I., Ding,L., Huebner,N., Mann,M. *et al.* (2011) RAD21 cooperates with pluripotency transcription factors in the maintenance of embryonic stem cell identity. *PLoS One*, **6**, e19470.
78. Schmidt,D., Schwalie,P.C., Ross-Innes,C.S., Hurtado,A., Brown,G.D., Carroll,J.S., Flicek,P. and Odom,D.T. (2010) A CTCF-independent role for cohesin in tissue-specific transcription. *Genome Res.*, **20**, 578–588.
79. Liu,N.Q., Maresca,M., van den Brand,T., Braccioli,L., Schijns,M., Teunissen,H., Bruneau,B.G., Nora,E.P. and de Wit,E. (2021) WAPL maintains a cohesin loading cycle to preserve cell-type-specific distal gene regulation. *Nat. Genet.*, **53**, 100–109.
80. Schwab,K.R., Patel,S.R. and Dressler,G.R. (2011) Role of PTIP in class switch recombination and long-range chromatin interactions at the immunoglobulin heavy chain locus. *Mol. Cell. Biol.*, **31**, 1503–1511.
81. Ing-Simmons,E., Seitan,V.C., Faure,A.J., Flicek,P., Carroll,T., Dekker,J., Fisher,A.G., Lenhard,B. and Merkenschlager,M. (2015) Spatial enhancer clustering and regulation of enhancer-proximal genes by cohesin. *Genome Res.*, **25**, 504–513.
82. Thiecke,M.J., Wutz,G., Muhar,M., Tang,W., Bevan,S., Malysheva,V., Stocsits,R., Neumann,T., Zuber,J., Fraser,P. *et al.* (2020) Cohesin-dependent and -independent mechanisms mediate chromosomal contacts between promoters and enhancers. *Cell Rep.*, **32**, 107929.
83. Mayayo-Peralta,I., Gregoricchio,S., Schuurman,K., Yavuz,S., Zaalberg,A., Kojic,A., Abbott,N., Geverts,B., Beerthuijzen,S., Siefert,J. *et al.* (2023) PAXIP1 and STAG2 converge to maintain 3D genome architecture and facilitate promoter/enhancer contacts to enable stress hormone-dependent transcription. *Nucleic Acids Res.*, gkad267.
84. Huang,J., Hsu,J.M. and Laurent,B.C. (2004) The RSC nucleosome-remodeling complex is required for cohesin's association with chromosome arms. *Mol. Cell*, **13**, 739–750.
85. Lopez-Serra,L., Kelly,G., Patel,H., Stewart,A. and Uhlmann,F. (2014) The Scc2-Scc4 complex acts in sister chromatid cohesion and transcriptional regulation by maintaining nucleosome-free regions. *Nat. Genet.*, **46**, 1147–1151.
86. Zhang,S., Ubelmesser,N., Josipovic,N., Forte,G., Slotman,J.A., Chiang,M., Gothe,H.J., Gusmao,E.G., Becker,C., Altmuller,J. *et al.* (2021) RNA polymerase II is required for spatial chromatin reorganization following exit from mitosis. *Sci. Adv.*, **7**, eabg8205.
87. Ba,Z., Lou,J., Ye,A.Y., Dai,H.Q., Dring,E.W., Lin,S.G., Jain,S., Kyritsis,N., Kieffer-Kwon,K.R., Casellas,R. *et al.* (2020) CTCF orchestrates long-range cohesin-driven V(D)J recombinational scanning. *Nature*, **586**, 305–310.
88. Seitan,V.C., Hao,B., Tachibana-Konwalski,K., Lavagnolli,T., Mira-Bontenbal,H., Brown,K.E., Teng,G., Carroll,T., Terry,A., Horan,K. *et al.* (2011) A role for cohesin in T-cell-receptor rearrangement and thymocyte differentiation. *Nature*, **476**, 467–473.
89. Thomas-Claudepierre,A.S., Schiavo,E., Heyer,V., Fournier,M., Page,A., Robert,I. and Reina-San-Martin,B. (2013) The cohesin complex regulates immunoglobulin class switch recombination. *J. Exp. Med.*, **210**, 2495–2502.
90. Zhang,X., Zhang,Y., Ba,Z., Kyritsis,N., Casellas,R. and Alt,F.W. (2019) Fundamental roles of chromatin loop extrusion in antibody class switching. *Nature*, **575**, 385–389.
91. Bot,C., Pfeiffer,A., Giordano,F., Manjeera,D.E., Dantuma,N.P. and Ström,L. (2017) Independent mechanisms recruit the cohesin loader protein NIPBL to sites of DNA damage. *J. Cell Sci.*, **130**, 1134–1146.
92. Callen,E., Di Virgilio,M., Kruhlak,M.J., Nieto-Soler,M., Wong,N., Chen,H.T., Faryabi,R.B., Polato,F., Santos,M., Starnes,L.M. *et al.* (2013) 53BP1 mediates productive and mutagenic DNA repair through distinct phosphoprotein interactions. *Cell*, **153**, 1266–1280.
93. Arnould,C., Rocher,V., Finoux,A.L., Clouaire,T., Li,K., Zhou,F., Caron,P., Mangeot,P.E., Ricci,E.P., Mourad,R. *et al.* (2021) Loop extrusion as a mechanism for formation of DNA damage repair foci. *Nature*, **590**, 660–665.
94. Ström,L., Lindroos,H.B., Shirahige,K. and Sjögren,C. (2004) Postreplicative recruitment of cohesin to double-strand breaks is required for DNA repair. *Mol. Cell*, **16**, 1003–1015.
95. Bailey,M.L., Tieu,D., Habsid,A., Tong,A.H.Y., Chan,K., Moffat,J. and Hieter,P. (2021) Paralogous synthetic lethality underlies genetic dependencies of the cancer-mutated gene STAG2. *Life Sci. Alliance*, **4**, e202101083.
96. van der Lelij,P., Newman,J.A., Lieb,S., Jude,J., Katis,V., Hoffmann,T., Hinterndorfer,M., Bader,G., Kraut,N., Pearson,M.A. *et al.* (2020) STAG1 vulnerabilities for exploiting cohesin synthetic lethality in STAG2-deficient cancers. *Life Sci. Alliance*, **3**, e202000725.
97. Ray Chaudhuri,A., Callen,E., Ding,X., Gogola,E., Duarte,A.A., Lee,J.E., Wong,N., Lafarga,V., Calvo,J.A., Panzarino,N.J. *et al.* (2016) Replication fork stability confers chemoresistance in BRCA-deficient cells. *Nature*, **535**, 382–387.